Cassini Orbiter Radio Science Subsystem Occultation and Electron Density at Titan: User Guide

Paul Withers (withers@bu.edu, Boston University)

and Paul Dalba (Boston University)

Version 1.0

1 September 2020

Contents

List of Tables

List of Figures

1 Scope

This user guide describes derived data products from Cassini radio occultations at Titan and their accompanying documentation. Derived data products include: (A) time series of the frequency of the radio signal received at Earth during an occultation (freq); (B) individual electron density profiles from occultations (indn); (C) average electron density profiles from occultations (aven); and (D) summary of average electron density profiles (summ). Since each occultation event was observed by multiple Deep Space Network antennas, here an individual electron density profile refers to results based on observations at a single antenna and an average electron density profile refers to the average profile from all available observations of an occultation event.

Note that this document is effectively divided into four parts. Sections 2–8 describe the generation and validation of the derived data products. Sections 9–11 are PDS-specific. They describe archive organization, data product formats, and naming conventions. Section 12 derives a useful mathematical result. Sections 13–16 contain acknowledgements, references, tables, and figures.

The structure of this document is as follows. Section 2 introduces the document. Section 3 describes the available raw data. Section 4 describes how frequency is determined from raw data for occultations at Titan. Section 5 describes how slant profiles of integrated column density at Titan are obtained from time series of frequency. Section 6 describes how individual vertical profiles of electron density at Titan are obtained from slant profiles of integrated column density. Section 7 describes how an average electron density profile at Titan is obtained from a set of individual electron density profiles. Section 8 discusses the validation of the Titan ionospheric observations. Section 9 describes the archive organization. Section 10 describes the format of archived data products. Section 11 describes the file naming conventions. Section 12 derives a useful mathematical result. Section 13 gives acknowledgements. Section 14 lists references. Section 15 contains tables. Section 16 contains figures.

A version of this document was peer-reviewed and published as *Dalba and Withers* (2019).

There is extensive overlap between the contents of this document and the contents of *Dalba and Withers* (2019).

2 Introduction

The Cassini spacecraft operated in the Saturn system from Saturn orbit insertion in 2004 until its destruction in Saturn's atmosphere in 2017. Its scientific payload included the Radio Science Subsystem (RSS) (*Kliore et al.*, 2004). The investigations conducted by the RSS instrument included radio occultation observations of the atmospheres and ionospheres of Saturn (*Nagy et al.*, 2006; *Moore et al.*, 2006; *Del Genio et al.*, 2009; *Nagy et al.*, 2009; *Schinder et al.*, 2011a, 2015), Titan (*Kliore et al.*, 2008, 2011; *Cravens et al.*, 2010; *Flasar et al.*, 2010; *Strobel et al.*, 2010; *Schinder et al.*, 2011b, 2012; *Tokano*, 2014), and Enceladus (*Kliore et al.*, 2006, 2010a,b,c, 2013; *Schinder et al.*, 2015). In radio occultation observations, a radio signal is transmitted between the spacecraft and a ground station such that the radio signal passes through the atmosphere and ionosphere of a target object. Propagation through the environment of the target object affects the received properties of the radio signal (e.g., *Withers*, 2010, and references therein). The distance of closest approach of the ray path to the target object changes with time due to spacecraft motion. Consequently, vertical profiles of neutral atmospheric density, pressure, and temperature and ionospheric electron density can be determined from analysis of time series of properties of the received radio signal during an occultation (e.g., *Eshleman*, 1973; *Withers et al.*, 2014, and references therein).

During a radio occultation, Cassini transmitted radio signals at up to three frequencies (S-band at 2.3 GHz, X-band at 8.4 GHz, and Ka-band at 32 GHz). All three downlink signals were coherently related. That is, they were generated by the same source. This source was an onboard ultrastable oscillator (USO) prior to its failure in December 2011 (*Schinder et al.*, 2015) and an uplinked single frequency radio signal after 2011. At Titan, occultations up to T057 used the USO, occultations from T101 onwards used an uplink signal. For the work reported here, it does not matter which source was used. The point of using a single signal

generator is that the three transmitted frequencies are precisely related: $f_{T,X}/f_{T,S} = 11/3$ and $f_{T,Ka}/f_{T,X} = 4$ (*Kliore et al.*, 2004). These relationships in the transmitted frequencies permit simple analysis techniques to be applied to the received frequencies (Section 5).

At the time of writing, the complete set of neutral atmospheric and ionospheric profiles from Cassini radio occultation observations at Titan has not been published. Publication and archiving of this complete set of profiles is critical for the success of the Cassini radio science investigation. Furthermore, making this complete set of profiles publicly available will be valuable for a wide range of scientific studies of the Saturn system. The aim of this archive is to disseminate one component of this set, all ionospheric electron density profiles from Cassini radio occultation observations at Titan. We also report on the successful preprocessing of raw data from Cassini radio occultation observations at Titan. The derived Titan ionospheric electron density profiles and derived time series of received frequency during Titan occultations are included in this archive.

We prioritized determination of ionospheric profiles over neutral atmospheric profiles because they can be obtained directly from time series of received frequencies without the need to determine the small difference, known as the frequency residual, between actual received frequency and the frequency that would have been received in the absence of any atmosphere and ionosphere around the target object (e.g., *Kliore et al.*, 2004; *Pätzold et al.*, 2004). It is challenging to determine accurately the mHz frequency residual from the GHz received frequency (e.g., *Pätzold and thirty colleagues*, 2009; *Schinder et al.*, 2015). Furthermore, Cassini RSS team member Paul Schinder is actively working to determine neutral atmospheric profiles from radio occultation observations (*Schinder et al.*, 2011a,b, 2012, 2015).

We prioritized the processing of observations from Titan over Saturn because the oblateness of Saturn introduces complexities to the data processing that are not present at spherical Titan (e.g., *Schinder et al.*, 2015). We prioritized Titan over Enceladus because of a desire to verify our data processing methods on a reasonably well-characterized ionosphere, rather than the highly variable and highly structured plasma plumes of Enceladus. In future work, we intend to determine ionospheric electron density profiles from Cassini radio occultation

observations at Saturn and Enceladus.

Cassini's radio occultation observations at Titan are labeled "TAAAB" where "AAA" is a number that uniquely identifies a given flyby of Titan and "B" is either "N" for an ingress occultation or "X" for an egress occultation. We generated Titan ionospheric electron density profiles for twenty occultations. Of these, eight (T012N, T012X, T014N, T014X, T027N, T027X, T031N, T031X) are validated by comparison to versions previously archived by the Cassini RSS team (*Kliore and Barbinis*, 2010) and five (T046N, T046X, T052N, T052X, T057N) are validated by comparison to images in publications by the Cassini RSS team (*Kliore et al.*, 2008, 2011). The remaining seven Titan ionospheric profiles (T101N, T101X, T102N, T102X, T117N, T117X, T119X) have not been reported previously. We anticipate that these profiles will be valuable for a wide range of studies of Titan's environment and its interaction with Saturn's magnetosphere.

Titan's ionosphere is part of the boundary between the satellite and Saturn's magnetosphere. Consequently, it is influenced by the bombardment of Titan by charged magnetospheric particles, which makes ionospheric properties dependent on the ram direction. Titan's ionosphere is important for many processes that lead to the escape of ion and neutral species. Ionospheric chemistry is intimately connected with the chemistry of the neutral atmosphere, and is also important in the production of haze particles, tholins, and the organic materials present on Titan's surface (from where they may be processed into the interior and its subsurface ocean). In particular, production of N-bearing species invariably involves the ionosphere, since most mechanisms for breaking the strong N_2 bond result in the formation of ions (*Cravens et al.*, 2010).

Ionospheric electron density profiles from radio occultations are generally characterized by excellent vertical resolution and excellent absolute calibration. At Titan, Cassini's radio occultation electron density profiles extend to altitudes below those that have been sampled by Cassini's in situ instruments (e.g., *Ågren et al.*, 2009). Only one prior radio occultation electron density profile exists for Titan, where the extraction of a single profile from observations made during the Voyager 1 flyby required nearly two decades of analysis (*Bird et al.*,

1997).

At Titan, Cassini electron density profiles have been used to discover that the vertical distribution of ionospheric plasma is characterized by a main peak at 1200 km and a lower, weaker, and variable peak at 500–600 km, to investigate differences between the dawn and dusk ionospheres, and to constrain the relative importance of ion production by solar photons and by electrons from Saturn's magnetosphere (*Kliore et al.*, 2008, 2011; *Cravens et al.*, 2010). The observations reported herein can be used to test predictions of ionospheric chemistry, structure, dynamics, and energetics, and of how solar photons and precipitating magnetospheric electrons produce plasma.

3 Available raw data

Radio signals transmitted by Cassini during radio occultations were received on Earth by antennas of the NASA Deep Space Network (DSN) and recorded on specialized Radio Science Receivers (RSRs). Relevant data from Cassini's radio occultations are archived on the NASA Planetary Data System (PDS) in "Radio Science Receiver" (RSR) files. The received radio signal is known as the "sky frequency". It has a frequency in the GHz range, which is much higher than is convenient for recording. At the ground station, several processing or mixing steps occur prior to recording. Effectively, three known frequencies are subtracted from the sky frequency. First, a known frequency in the GHz range is subtracted to yield an observed frequency in the MHz range. Second, a known frequency in the MHz range is subtracted to yield an observed frequency in the kHz range. Third, a known frequency in the kHz range is subtracted to yield an observed frequency in the Hz range. The end-product of these steps is called the "mixed-down" signal. The sky frequency can be found by summing the frequency of the mixed-down signal and the three known mixing frequencies.

The archived RSR data products are based on the mixed-down signal, which has a frequency in the Hz range. The key data products are time series of "I/Q pairs" of the mixed-down signal. These can be described by an analogy. The arriving electromagnetic signal has

an amplitude and a phase, as does a complex number. A complex number can be expressed as a real part and an imaginary part, which are determined by the amplitude and phase. The in-phase signal, I, is analogous to the real part and the quadrature signal, Q, is analogous to the imaginary part.

Figure 1 shows an example of two seconds of I/Q data recorded at X-band at Deep Space Network Station 14 (DSS-14), a 70m antenna at Goldstone, during the T012X occultation on 19 March 2006. In this example, the frequency of the mixed-down signal is obviously on the order of either -2 Hz or +2 Hz. Since oscillations in I lead oscillations in Q, the frequency is positive.

As of 02 April 2017, 940 RSR data files from Cassini radio occultations of the atmospheres and ionospheres of Saturn, Titan, and Enceladus were archived at the PDS Atmospheres Node (http://atmos.nmsu.edu/data_and_services/atmospheres_data/Cassini/rss.html). These include measurements at S-band (2.3 GHz), X-band (8.4 GHz), and Ka-band (32 GHz) frequencies (*Kliore et al.*, 2004). These files are organized into volumes. We acquired copies of all RSR data files for which the "experiment name" contained "occ"

(http://atmos.nmsu.edu/data_and_services/atmospheres_data/Cassini/logs/

RSS/Datasets/180330.html). Note, however, that this listing may be incomplete. Browsing the archive structure directly can reveal occasional omissions. We acquired copies of the data files in the following volumes: ENOC1 and ENOC2 (Enceladus, up to 26 January 2010); SROC1–21 (Saturn, up to 30 June 2016); and TOCC1 and TBOC1–8 (Titan, up to 06 May 2016). Additional RSR data files for Saturn occultations were archived after May 2017 (SROC22, SROC23, SROC24, SROC25), but were not incorporated into this analysis. Furthermore, more RSR data files may be archived in the future from the terminal phase of the Cassini mission. In almost all acquired files, data are reported at 16,000 samples per second. There are fifteen exceptions from Saturn occultations in mid-2008 that are reported at 2000 samples per second. Due to their reduced sampling rate, these fifteen RSR data files are noticeably smaller in size than is typical.

In the current work, we process, archive, and discuss only those RSR data files that are

right-circular polarized and associated with Titan occultations. We set aside left-circular polarized data as Cassini transmitted right-circular polarized radio signals and occultations do not generally affect polarization.

4 Determination of frequencies

The frequency of the received radio signal, which is the critical foundation of the data analysis procedure, is derived from the I/Q pairs. A time series of complex numbers is formed from the I/Q pairs, which is then subjected to a Fourier transform. The frequency at which the resultant power spectrum is maximized is the frequency of the arriving radio signal. However, finding this frequency to adequate accuracy is not trivial. We consider the time resolution required to achieve the desired vertical resolution, appropriate frequency accuracy, and numerical methods that can provide them.

The sampling rate at which frequency should be determined depends on the desired vertical resolution. The theoretical limit of the vertical resolution for radio occultation observations analyzed using the assumptions of geometric optics (i.e., diffraction is neglected) is $2\sqrt{\lambda D}$ (*Karayel and Hinson*, 1997; *Hinson et al.*, 1999), where λ is the wavelength of the radio signal and D is the distance between the spacecraft and the limb of the target object. We assume that D is on the order of the radius of the target object, although D is usually a few times larger than this. Therefore the theoretical limits of the vertical resolution at Titan are 1.2 km (S-band), 610 m (X-band), and 310 m (Ka-band).

The length of time taken for the closest approach distance of the ray path to sweep through this vertical distance gives the desired interval between one frequency measurement and the next. In a typical Cassini occultation, the rate of change of closest approach distance is 4.5 km s^{-1} at Titan (found from inspection of the Cassini trajectory). We adopt a time resolution of 1 second, which provides appropriate vertical resolution at Titan.

We estimate the frequency accuracy required to achieve the desired electron density accuracy using the relationships obtained for one-way, single-frequency occultation by *With-*

ers (2010). Although Cassini performs two-way, multi-frequency occultations, this estimate should be sufficient for planning purposes. Uncertainties σ_N in electron density N and σ_f in frequency f are related by (*Withers*, 2010):

$$\sigma_f = \frac{V \sigma_N e^2}{8\pi^2 c m_e \epsilon_0 f} \sqrt{\frac{2\pi R}{H}} \tag{1}$$

Here V is Cassini's speed (more precisely, the rate of change of the closest approach distance), $-e$ is the electron charge, c is the speed of light, m_e is the electron mass, ϵ_0 is the permittivity of free space, f is the frequency, R is the tangent distance of the ray path, and H is the plasma scale height in the ionosphere.

Representative values for Titan are $V = 4.5$ km s^{-1} (found from inspection of the Cassini trajectory), $R = 3775$ km (*Kliore et al.*, 2008), and $H = 200$ km (*Cravens et al.*, 2010). *Kliore et al.* (2008) reported electron density uncertainties of $\sim$100 cm^{-3}. However, these uncertainties apply to the average of multiple individual profiles. Cassini used multiple antennas to observe a given occultation. Data from each antenna yielded an independent electron density profile, and these were averaged to generate the reported profile. With four independent profiles, the uncertainty in the average profile is reduced from the uncertainty in an individual profile by a factor of $\sqrt{4}$. In reality, the assumption that the noise at each antenna is independent is over-simplified. Fluctuations in the solar wind will have essentially the same effect on each individual profile. The same is true for the terrestrial ionosphere for antennas at the same DSN complex. However, this assumption is sufficient for the current purpose of projecting uncertainties. We therefore adopt a target uncertainty of 200 cm^{-3}. We adopt $f = 2.3$ GHz, since the low-frequency S-band signals are most sensitive to plasma, and find $\sigma_f = 0.57$ mHz.

This corresponds to a frequency stability of $\sim 2 \times 10^{-13}$, consistent with the performance of the Cassini ultrastable oscillator (USO) at a time interval of 1 second (*Kliore et al.*, 2004). A benefit of mixing down the signal is that its frequency must be determined to $\sim$1 part in 10^3 (millihertz accuracy on $\sim$1 Hz signal), rather than $\sim$1 part in 10^{12} (millihertz accuracy on $\sim$GHz signal).

Therefore we require frequencies to be determined with an accuracy of 0.5 mHz and a sampling interval of 1 second from time series of I/Q data reported at a rate of 16,000 samples per second. However, the nominal accuracy with which the frequency of time series data can be found is no better than the reciprocal of the duration of the time series (the Nyquist limit) (e.g., *Press et al.*, 1988). In this case, it appears that millihertz resolution requires >1700 seconds (>30 minutes) of data, much longer than the targeted sampling interval of 1 second and longer, in some cases, than the full duration of the radio occultation.

This is an example of a common problem in signal processing and numerous techniques exist for resolving it. Six approaches are listed in the Cassini Radio Science User's Guide (Asmar et al., 2018,

https://atmos.nmsu.edu/data_and_services/atmospheres_data/Cassini/inst-rss.html).

One of the simplest is "zero padding" in which a vast number of zeros are added to a short time series to make it longer. The theoretical limit on the frequency resolution then equals the ratio of the sampling rate (16,000 samples per second) to the number of elements in the padded time series. Thus padding a set of 16,000 measured data points with zeroes until the set contains 2^{25} values, approximately 3.4×10^7, can provide resolution of 0.48 mHz, which satisfies the stated requirement of 0.5 mHz. We restrict possible padding lengths to powers of two in order to increase the computational efficiency with which the Fourier transform is performed (e.g., *Press et al.*, 1988).

The padded set of I/Q data points is then subjected to a Fourier transform to generate its power spectrum. An example is shown in Figure 2. The frequency of the mixed-down radio signal is the frequency at which the power spectrum is maximized. As suggested by inspection of the I/Q data in Figure 1, the frequency is around +2 Hz. Zero padding introduces spectral artefacts, which are visible in Figure 2, but these are not a problem. They are typically additional smaller peaks in the power spectrum that are shifted from the main peak by integer multiples of $1/T$, where T is the 1 second duration of the actual data series. Hence peaks are separated by 1 Hz. Figure 2 also shows the power spectrum of the set of I/Q data points without zero padding. Only a single peak is present, but the separation

between adjacent frequency values is also 1 Hz, which is far too coarse to be useful for our purposes.

Figure 3 shows an example of a full time series of mixed-down frequency measurements. Clearly, not all these frequency measurements are realistic. At 1000 seconds, Cassini is occulted by Titan as viewed from Earth and the received radio signal is merely antenna noise. At early and late times, Cassini is either not transmitting in the relevant frequency band or its high-gain antenna is not pointed towards Earth. Figure 4 shows the corresponding time series of the square of the absolute value of the Fourier transform at the relevant frequency. In addition to these features, there are fluctuations in both frequency and power around 600 seconds and 1400 seconds. The earlier of these two periods corresponds to the gradual loss of the radio signal by the receiver upon ingress. The later of these two periods is its egress counterpart.

Frequency measurements at Titan were classified as to their suitability for use in occultation analysis. At Titan, a mixed-down frequency measurement was deemed reliable when (A) the mixed-down frequency was stable over time and (B) the square of the absolute value of the Fourier transform was large and stable over time. Based on manual evaluation of these criteria, frequency measurements were classified as "suitable for use in ingress occultation", "suitable for use in egress occultation", or "not suitable". This information is represented by quality flags in the frequency data products we generated. In this example, frequency measurements at approximately 200–500 seconds were classified as "suitable for use in ingress occultation". Frequency measurements at approximately 1400–3200 seconds were classified as "suitable for use in egress occultation".

Figure 5 shows how the derived mixed-down frequency depends on the zero-padding for a period of time when the ray path does not encounter any atmosphere or ionosphere in the Saturn system. In principle, the mixed-down frequency should vary smoothly with time here. Discretization of the derived mixed-down frequency is visible, with the separation between adjacent discrete values being larger for shorter padding lengths. Note that Figures 3–4 reference time to the start of time series of frequency measurements, whereas Figure 5

and subsequent figures reference time to the start of the subset of frequency measurements classified as suitable for use in egress occultation. Hence a time of zero in Figure 5 and subsequent figures corresponds to a time of 1439 seconds in Figures 3–4.

Figure 6 shows how the root-mean-square of the difference between the derived mixed-down frequency and a quadratic fit depends on the zero-padding. The root-mean-square difference decreases as the length of padding increases, but asymptotically approaches a threshold value. This threshold is close to the 1.8 mHz accuracy expected for an 8.4 GHz (X-band) signal generated by the Cassini USO, which has an Allan deviation of 2×10^{-13} at a time interval of one second (*Kliore et al.*, 2004).

The actual received frequency (GHz range) was determined by adding the mixed-down frequency found from the power spectrum (Hz range) to the known reference mixing frequencies, which are included in the archived RSR files. We generated time series of received frequency for the 84 archived RSR files from Cassini radio occultations that are at right-circular polarization and that are associated with Titan occultations. This set of data products is included in this archive. Note that all derived frequency measurements were delivered, not just those classified as realistic.

Note also that an error in the header of RSR files is common for files that contain data from 01 January 2010 or later (SROC11 and greater). The number of rows stated in the header (ROWS) is a factor of 4 too small. ROWS should be four times greater than the total duration of the RSR observation (STOP_TIME - START_TIME) in seconds. In these erroneous cases, ROWS equals the total duration of the RSR observation (STOP_TIME - START_TIME) in seconds.

5 From time series of frequency to slant profiles of integrated column density at Titan

A time series of the frequency of the received radio signal during an occultation contains information about the ionospheric electron densities at the target object. In the non-relativistic

limit, the received frequency of a radio signal, f_R, is related to the transmitted frequency, f_T, as follows (Withers, 2010; Withers et al., 2014):

$$f_R = f_T - \frac{f_T}{c}\frac{d}{dt}\int dl + \frac{e^2}{8\pi^2 m_e \epsilon_0 c f_T}\frac{d}{dt}\int N dl - \frac{f_T \kappa}{c}\frac{d}{dt}\int n dl \tag{2}$$

Here t is time, l is the path length, c is the speed of light, $-e$ is the electron charge, m_e is the electron mass, ϵ_0 is the permittivity of free space, N is the electron density at a given point, κ is the refractive volume of neutral gas at a given point, and n is the neutral density at a given point. Three terms on the right-hand side cause the received frequency, f_R, to differ from the transmitted frequency, f_T. From left to right, they are the classical Doppler shift, a shift due to plasma along the ray path, and a shift due to neutral gas along the ray path.

During a radio occultation, Cassini transmitted at multiple frequencies. All downlink signals were coherently related and generated from the same frequency source. Consequently, the transmitted frequencies are precisely related: $f_{T,X}/f_{T,S} = 11/3$ and $f_{T,Ka}/f_{T,X} = 4$ (*Kliore et al.*, 2004). Due to frequency shifts along the ray path (Equation 2), the received frequencies are not so simply related, but these relationships in the transmitted frequencies permit simple analysis techniques to be applied to the received frequencies.

In this description, we consider S-band and X-band signals. Extension to other pairs of frequencies is trivial. Note in Equation 2 that the classical Doppler shift and the shift due to neutral gas are proportional to the frequency, but the shift due to plasma is inversely proportional to the frequency. Therefore, since the ratio of the frequency at which the downlinked S-band signal was transmitted to the frequency at which the downlinked X-band signal was transmitted is a known constant, 3/11, the S-band and X-band versions of Equation 2 can be rearranged and combined to yield:

$$f_{R,S} - \left(\frac{3}{11}\right) f_{R,X} = \frac{e^2}{8\pi^2 m_e \epsilon_0 c f_{T,S}} \left(1 - \left(\frac{3}{11}\right)^2\right) \frac{d}{dt}\int N dl \tag{3}$$

This result also holds in the relativistic case where all non-plasma-related shifts are

proportional to frequency (*Pätzold et al.*, 2004; *Schinder et al.*, 2015; *Bocanegra-Bahamón et al.*, 2018). Consequently, the rate of change of the plasma column density along the ray path can be determined straight-forwardly from time series of the received frequency at two different frequency bands. However, it should be noted that the cancelation of the non-dispersive terms implied by Equation 3 is imperfect. Equation 3 assumes that both radio signals follow identical ray paths. Since the refractive index of plasma is frequency-dependent, the two radio signals actually follow slightly different paths. In common with other investigators, we neglect this.

Equation 3 is the key equation linking desired environmental properties (N, electron density) to measured quantities (f, received frequency). Figure 7 shows how the presence of plasma is readily visible in a time series of the weighted difference of the received frequencies, but not the individual frequencies. Recall from Section 4 that a time of zero in Figure 7 and subsequent figures corresponds to a time of 1439 seconds in Figures 3–4.

Data with the appropriate ingress or egress quality flag were selected from the full time series of frequency observations. Next, outlier values of $f_{R,S} - 3f_{R,X}/11$ were manually identified and replaced by interpolation between neighboring values. Outlier values occurred rarely, no more than a few in any single observation and in only a small fraction of all observations. They were generally ten or more standard deviations away from the main cluster of values.

At either the start of an ingress occultation or the end of an egress occultation, the closest approach of the ray path to the center of Titan is thousands of kilometers above the ionosphere of Titan. Since there should be no ionospheric plasma along the ray path, the quantity $f_{R,S} - 3f_{R,X}/11$ should be zero for this period of time. However, changes with time in the contribution to the plasma column density from plasma in Earth's ionosphere or the interplanetary medium, can cause it to be non-zero. This possible problem is addressed by selecting a period of time where ray paths have high-altitude closest approach points, fitting a time series of $f_{R,S} - 3f_{R,X}/11$ from that period to a low-order polynomial function of time, then subtracting this fitted "baseline trend" from the entire duration of the dataset.

Integration of the baseline-corrected time series of $f_{R,S} - 3f_{R,X}/11$ with respect to time, assumption of a suitable constant of integration, and multiplication by the factor present in Equation 3 yields the column density of plasma along the ray path as a function of time. The absolute total column density, which includes plasma in Earth's ionosphere and the interplanetary medium, is neither known nor required. For convenience, we chose a constant of integration such that the column density is zero at the start of the time series. For ingress observations, that is at high altitude above the ionosphere. For egress observations, that is at low altitude below the ionosphere.. As shown in Figure 8, we now have the column density of ionospheric plasma along the ray path as a function of time

Time is no longer useful as the independent variable for this data product, and the next step is to replace it with the closest approach distance of the relevant ray path to the center of mass of Titan. This is performed using the JPL NAIF SPICE tools. Bending of the ray path within the ionosphere does not need to be considered, since bending only becomes significant in the neutral atmosphere, which is much more refractive than the ionosphere. According to the relationships in *Withers* (2010), rays that encounter the ionosphere, but not the neutral atmosphere, are bent by less than 10^{-6} radians. At a distance of 10 Titan radii, that corresponds to a distance of 26 m, much smaller than relevant ionospheric lengthscales. At this stage, we now have the column density of ionospheric plasma along the ray path as a function of closest approach distance (Figure 9).

6 From slant profiles of integrated column density to vertical profiles of electron density at Titan

As ionospheric refractivity is small at GHz frequencies, radio signals from Cassini that pass through Titan's ionosphere, but not its atmosphere, propagate through Titan's environment in a straight line. This simplifies the determination of local electron density. For straight ray paths through a spherically symmetric ionosphere, we have (e.g., *Quémerais et al.*, 2006):

$$\Omega(X) = 2\int_{r=X}^{r=\infty} \frac{Nrdr}{\sqrt{r^2 - X^2}} \tag{4}$$

Here Ω is the column density of ionospheric plasma along the ray path and X is the closest approach distance. In the special case where N decreases exponentially with increasing radial distance, r, then $\Omega(r) = N(r)\sqrt{2\pi r H}$, where H is the scale height (Section 12). In general, Equation 4 can be inverted via an Abel transform to yield Equations 5 and 6 (e.g., *Fjeldbo et al.*, 1971; *Hinson et al.*, 1999; *Withers*, 2010):

$$N(r) = \frac{-1}{\pi}\int_{X=r}^{X=\infty} \frac{d\Omega(X)}{dX}\frac{dX}{\sqrt{X^2 - r^2}} \tag{5}$$

$$N(r) = \frac{1}{\pi}\int_{X=r}^{X=\infty} \ln\left(\frac{X}{r} + \sqrt{\left(\frac{X}{r}\right)^2 - 1}\right) d\left(\frac{d\Omega(X)}{dX}\right) \tag{6}$$

Hence a vertical ionospheric electron density profile, $N(r)$, can be found from the function $\Omega(X)$. Note also that the electron density profile $N(r)$ depends only on the derivative $d\Omega(X)/dX$. As previously noted, the constant of integration that fixes the absolute values of Ω is not significant for resultant electron density profiles. The method used to solve Equation 6 ensured that the electron density was zero at the highest altitude in each profile.

We distinguish between individual and average electron density profiles. Cassini transmits at up to three frequencies, each DSN complex has multiple antennas, and multiple DSN complexes may be visible from Cassini at the time of an occultation. For example, the T012X occultation was observed at DSS-14 (a 70-meter antenna at Goldstone) in S-band and X-band, DSS-25 (34m, Goldstone) in X-band and Ka-band, DSS-26 (34m, Goldstone) in X-band and Ka-band, and DSS-63 (70m, Madrid) in S-band and X-band. Hence multiple independent electron density profiles can be determined for a single occultation. An individual electron density profile is derived as outlined above from radio occultation observations at two frequencies at a single antenna; an average profile is an average of the multiple independent individual electron density profiles that can be determined for a single occultation (Section 7).

Figure 10 shows an individual electron density profile determined for the T012X occultation (19 March 2006) using the S-band and X-band signals received at DSS-14, a 70-meter antenna at Goldstone. Figure 10 also shows the average electron density profile determined for this occultation by the Cassini RSS team, which was previously archived at the PDS (*Kliore and Barbinis*, 2010). The two versions of this profile are reasonably similar, which suggests that our methods are sound. Differences are discussed further in Section 7.

Uncertainties must be assigned to the derived electron densities. For each individual electron density profile, we find the standard deviation of all electron density measurements above a threshold altitude. Altitude, z, is defined as the difference between radial distance, r and the radius of Titan, 2575 km. Mean electron densities at high altitudes are sufficiently close to zero that root-mean-square densities are not significantly larger than the standard deviation of the densities. The typical threshold altitude was 1500–2000 km. This value was selected manually for each profile in order to maximize the length of the baseline whilst excluding any significant ionospheric features. The typical threshold altitude can be justified independently from the radio occultation observations. Cassini RPWS Langmuir probe in situ measurements of electron density show that electron densities are less than 100 cm^{-3}, the characteristic electron density uncertainty found by *Kliore et al.* (2008) (Section 4), above 2000 km (*Ågren et al.*, 2009; *Coates et al.*, 2011; *Edberg et al.*, 2015). The standard deviation of electron densities at high altitude is assigned as the uncertainty for each electron density measurement in the profile. Hence the uncertainty in electron density in a given individual electron density profile does not vary with altitude. The uncertainty in the T012X individual profile shown in Figure 10 is about 330 cm^{-3}, consistent with the target uncertainty of 200 cm^{-3} (Section 4).

Figure 11 shows how the electron density uncertainty depends on the zero-padding length adopted in Section 4. Based on the trends shown here, increase in the padding length beyond the adopted 2^{25} elements would not improve the electron density uncertainty significantly.

All individual electron density profiles are included in this archive. We generated 66 profiles for twenty occultations from eleven Titan flybys. Raw data are available for ingress

on the T57 flyby, but not egress, and for egress on the T119 flyby, but not ingress.

7 From individual electron density profiles to an average electron density profile at Titan

The individual electron density profiles from a single occultation are all different, even though they all sample the same region of Titan's ionosphere. An example is shown in Figure 12. Possible causes of these differences are antenna-specific and receiver-specific noise, and different paths through Earth's ionosphere. The path through Earth's ionosphere matters because an individual electron density profile is derived from a time series of total electron content measurements. Although the average contribution from Earth's ionosphere will be removed by the baseline correction, time variations in the total electron content contribution from Earth's ionosphere along this line-of-sight will affect the resultant electron density profile. Differences caused by Earth's ionosphere will be most significant when comparing profiles based on observations made at different DSN complexes ($\sim$10,000 km and many hours of local time apart), but could also be present when comparing profiles based on observations made at different antennas at the same DSN complex (<10 km apart).

These individual profiles can be combined to yield an average electron density profile with smaller uncertainties. For each occultation, we trim the set of individual profiles so that all span the same altitude range. The average electron density N has uncertainty σ, where N and σ satisfy $N/\sigma^2 = \Sigma N_i/\sigma_i^2$ and $1/\sigma^2 = \Sigma 1/\sigma_i^2$. Here N_i are densities from individual profiles and σ_i are the corresponding uncertainties. This approach for the calculation of uncertainties assumes that noise in the individual electron density profiles is independent. This assumption is appropriate for thermal noise at each DSN antenna. However, fluctuations in the solar wind will have essentially the same effect on each individual profile. The same is true for the terrestrial ionosphere for antennas at the same DSN complex. Nevertheless, we adopt the assumption of independence when calculating uncertainties in order to maintain consistency with the weighted calculation of the average electron density values themselves.

An alternative approach would be to consider the standard deviation in high-altitude values of average electron density. For the T12 egress occultation and the T57 occultation, this yields an uncertainty that is 50% larger than that reported in the data products. Data users may wish to examine the standard deviation in high-altitude values of average electron density prior to accepting the reported uncertainty values.

With our adopted approach, an average profile generally covers a narrower altitude range than the constituent individual profiles, but has smaller uncertainties. This is shown in Figure 12. The T119X profile is a special case — only one individual profile exists, which was derived from S-band and X-band measurements. Here densities and uncertainties in the "individual" and "average" profiles are identical.

A different averaging method was used by the Cassini RSS team (*Kliore et al.*, 2008). This method did not trim the individual profiles to a common altitude range, so average profiles generated by the Cassini RSS team will cover a wider range of altitudes than those reported in this archive. The method of the Cassini RSS team generated uncertainties that varied with altitude. These uncertainties were generally larger than those reported in this archive. For further details, readers are referred to *Kliore et al.* (2008).

Figure 13 compares average electron density profiles from our work and the previously archived Cassini RSS team's work for occultation T012X (*Kliore and Barbinis*, 2010). The agreement is excellent. The root-mean-square difference between the two versions of this profile is 240 cm^{-3}, whereas our uncertainty is 150 cm^{-3} and the average uncertainty in the previously archived profile is 230 cm^{-3} (*Kliore and Barbinis*, 2010). For consistency, users are advised to use profiles from one source (this work or *Kliore and Barbinis* (2010)), but not to use some profiles from one source and some profiles from the other source.

All twenty average electron density profiles are included in this archive.

8 Validation of results at Titan

We generated average electron density profiles for twenty Titan occultations. Of these twenty profiles, thirteen have been previously published in *Kliore et al.* (2008) and *Kliore et al.* (2011). Of those thirteen profiles, eight were previously archived on the PDS (*Kliore and Barbinis*, 2010). The dates, locations, and other relevant information about the profiles are summarized in Table 1. With one exception, all quantities are taken directly from the archived data products. The exception is the magnetospheric ram angle, which is calculated as the angular separation between the occultation location and the magnetospheric ram point at 0°N, 90°E. Tabulated values for the first thirteen occultations can be compared against equivalent tables in *Kliore et al.* (2008) and *Kliore et al.* (2011). Agreement is generally good, although the two T012 occultation observations are listed as 20 March 2006 in *Kliore et al.* (2008) and *Kliore et al.* (2011) in an apparent typographical error. The correct date is 19 March 2006.

All twenty average electron density profiles are shown in Figures 14–18. Previously archived profiles are shown for comparison where available. Uncertainties on average electron density profiles are generally 100–250 cm^{-3}, consistent with the desired accuracy used to design the data processing method in Section 4. Agreement between our profiles and the eight previously archived profiles (*Kliore and Barbinis*, 2010), is generally good, which builds confidence in the validity of those of our profiles for which official Cassini RSS profiles are not available. Agreement between our profiles and the five previously unarchived profiles (T046N, T046X, T052N, T052X, T057N) that are shown in figures and summarized in tables by *Kliore et al.* (2011) is also generally good.

On the whole, the main features of the new profiles are generally consistent with the main features of profiles previously reported by *Kliore et al.* (2008) and *Kliore et al.* (2011). Specifically, a single layer of plasma with peak density of 1000–3000 cm^{-3}, peak altitude of 1000–1300 km, and full-width at half maximum of a few hundred kilometers. This is consistent with Cassini in situ density observations (*Ågren et al.*, 2009).

9 Archive organization and naming

This section describes the basic organization of this archive, and the naming conventions used for the bundle, collection, and product logical identifiers.

9.1 Logical identifiers

Every product in PDS is assigned an identifier which allows it to be uniquely identified across the system. This identifier is referred to as a Logical Identifier or LID. A LIDVID (Versioned Logical Identifier) includes product version information, and allows different versions of a specific product to be referenced uniquely. A product's LID and VID are defined as separate attributes in the product label. LIDs and VIDs are assigned by the entity generating the labels and are formed according to the conventions described in Sections 9.1.1 and 9.1.2 below. The uniqueness of a product's LIDVID may be verified using the PDS Registry and Harvest tools.

9.1.1 LID formation

LIDs take the form of a Uniform Resource Name (URN). LIDs are restricted to ASCII lower case letters, digits, dash, underscore, and period. Colons are also used, but only to separate prescribed components of the LID. Within one of these prescribed components dash, underscore, or period are used as separators. LIDs are limited in length to 255 characters.

LIDs for products in this archive are formed according to the following conventions:

Bundle LIDs are formed by appending a bundle-specific ID to the base ID:

`urn:nasa:pds:<bundle ID>`

Since all PDS bundle LIDs are constructed this way, this bundle-specific ID must be unique across all bundles archived with the PDS.

Collection LIDs are formed by appending a collection-specific ID to the collection's parent bundle LID:

`urn:nasa:pds:<bundle ID>:<collection ID>`

Since the collection LID is based on the bundle LID, which is unique across PDS, the only additional condition is that the collection ID must be unique across the bundle. Collection IDs correspond to the collection type (e.g. "`browse`", "`data`", "`document`", etc.). Additional descriptive information may be appended to the collection type (e.g. "`data-raw`", "`data-calibrated`", etc.) to ensure that multiple collections of the same type within a single bundle have unique LIDs.

Basic product LIDs are formed by appending a product specific ID to the product's parent collection LID:

`urn:nasa:pds:<bundle ID>:<collection ID>:<product ID>`

Since the product LID is based on the collection LID, which is unique across PDS, the only additional condition is that the product ID must be unique across the collection.

9.1.2 VID formation

Product version ID's consist of major and minor components separated by a "." (M.n). Both components of the VID are integer values. The major component is initialized to a value of "1", and the minor component is initialized to a value of "0". The minor component resets to "0" when the major component is incremented.

9.2 Archive contents for the `corss_occul_el_dens` bundle

The Cassini Orbiter Radio Science Subsystem Occultation and Electron Density archive contains one bundle:

`urn:nasa:pds:corss_occul_el_dens`

There are two collections in this bundle:

`urn:nasa:pds:corss_occul_el_dens:data_derived` (a data collection)

`urn:nasa:pds:corss_occul_el_dens:document` (a document collection).

Product LIDs for a given collection are given in the portion of Section 9.2 that describes that collection. The following sections describe the contents of this bundle in greater detail.

9.2.1 `corss_occul_el_dens:data_derived` data collection

The `corss_occul_el_dens:data_derived` data collection contains four distinct types of products: (A) time series of the frequency of the radio signal received at Earth during an occultation (freq); (B) individual electron density profiles from occultations (indn); (C) average electron density profiles from occultations (aven); and (D) summary of average electron density profiles (summ). The generation and validation of each of these types of products is discussed earlier in this document.

9.2.2 Description of freq products

freq products contain time series of the frequency of the radio signal received at Earth during an occultation. They are ASCII files. Each frequency data product was generated from a single RSR file. An individual RSR file contains information about the radio signal in a specific frequency band. For Cassini, that is S, X, or Ka band. Cassini transmits with right circular polarization, but the DSN can record at left or right circular polarization. Note that a given RSR file may contain data from ingress alone, egress alone, or both ingress and egress. Hence a frequency data product also may contain data from ingress alone, egress alone, or both ingress and egress.

As outlined in Section 11.1, the file naming convention is:

`sssttaayyyyddd_hhmmxuudrrpq_rcs_freq_vxx_rxx.csv`

The product LID for this file is:

`sssttaayyyyddd_hhmmxuudrrpq_rcs_freq`

9.2.3 Description of indn products

indn products contain individual electron density profiles from occultations. They are ASCII files. Each individual electron density profile data product was generated from two frequency data products, where the two frequency data products were received simultaneously by the same Deep Space Network Station (DSS) in different frequency bands. We used frequency pairs S-band and X-band, and X-band and Ka-band, but not S-band and Ka-band. In no

instances did a given DSN antenna record S-band and Ka-band together. Inspection of Equation 3 shows that uncertainties in the rate of change of total electron content would be significantly worse for this frequency pair than for the other possible frequency pairs. Uncertainties in electron density would be significantly worse as well. Each individual electron density profile data product contains data from either ingress or egress, but not both.

As outlined in Section 11.2, the file naming convention is:

`sssttaayyyyddd_hhmm_t_bb_nn_ooooo_edp_vxx_rxx.csv`

The product LID for this file is:

`sssttaayyyyddd_hhmm_t_bb_nn_ooooo_edp`

9.2.4 Description of aven products

aven products contain average electron density profiles from occultations. They are ASCII files. Each average electron density profile data product was generated from every individual electron density profile data products that corresponds to a given observation (e.g., T012N, T031X). Each average electron density profile data product contains data from either ingress or egress, but not both. An average electron density profile data product may have been generated from individual electron density profile data products from different DSN complexes (e.g., Goldstone and Madrid for T012X). However, due to the great distance from Earth to Saturn relative to the size of Earth, these different individual profiles sample the same region in Titan's ionosphere. Thus it is reasonable to average them together.

As outlined in Section 11.3, the file naming convention is:

`sss_fffff_ooooo_edp_vxx_rxx.csv`

The product LID for this file is:

`sss_fffff_ooooo_edp`

9.2.5 Description of summ products

summ products contain a table that summarizes the observing conditions of all average electron density profile data products from a particular target object. They are ASCII files.

As outlined in Section 11.4, the file naming convention is:

`ooooo_summary_table_vxx_rxx.csv`

The product LID for this file is:

`ooooo_summary_table`

9.2.6 `corss_occul_el_dens:document` document collection

The `corss_occul_el_dens:document` document collection contains one distinct type of product: the user guide you are currently reading. This is a PDF/A document originally written in LaTeX.

The file naming convention is:

`userguide_vxx_rxx.pdf`

where

`vxx`: identifies the major component `xx` of the version number of this product

`rxx`: identifies the minor component `xx` of the version number of this product

The product LID for this file is:

`userguide`

Hence the complete LID is:

`urn:nasa:pds:corss_occul_el_dens:document:userguide`

10 Archive product formats

This section describes the format of each type of product in this archive.

The products that comprise this archive are formatted in accordance with PDS specifications, specifically: Planetary Data System Standards Reference, Version 1.8.0, 21 March 2017; PDS4 Data Dictionary — Abridged, Version 1.8.0.0, 10 March 2017; and Planetary Data System (PDS) PDS4 Information Model Specification, 1.8.0.0, 10 March 2017.

10.1 Data file formats

This section describes the format and record structure of each of the data file types (freq, indn, aven, summ). All data file types are archived as PDS4 Table_Delimited objects. They are ASCII files.

10.1.1 Structure of freq data files

Frequency data products are stored as comma-separated files and have the extension `.csv`. Each frequency data product contains ten time-ordered columns. The number of rows equals the ratio of the duration of the RSR file to the selected time resolution of 1 second.

Column 1: SFDU_YEAR. Dimensionless. ASCII_Integer (format code I10). UTC year for the SFDU data and models, where SFDU means "Standard Format Data Units". Values can range over 1900-3000. Corresponds to column number 47 in RSR file. See documentation of RSR files for further information.

Column 2: SFDU_DAY_OF_YEAR. Dimensionless. ASCII_Integer (format code I10). UTC day of year for the SFDU data and models. Values can range over 1-366. Corresponds to column number 48 in RSR file. See documentation of RSR files for further information.

Column 3: SFDU_SECOND. Unit=seconds. ASCII_Real (format code F20.3). UTC seconds of day for the SFDU data and models. Values can range over 0-86400. Corresponds to column number 49 in RSR files. See documentation of RSR files for further information.

Column 4: RF-IF_LO_FREQUENCY. Unit=megahertz (MHz). ASCII_Integer (format code I10). RF to IF Down Converter Local Oscillator (LO) Frequency. This specifies the total down-conversion applied to the signal before it entered the RSR DIG. The value is subtracted from the RF predict points in order to obtain the frequency of the desired signal at IF. The RSR selects a default value based on the downlink band: 2000 (S-Band), 8100 (X-Band), or 31700 (Ka-Band). This frequency is needed in order to reconstruct the sky frequency, FSKY, of the data contained in this SFDU: FSKY = RF-IF_LO_FREQUENCY + DDC_LO_FREQUENCY - NCO_FREQUENCY + MIXED-DOWN_FREQUENCY where RF-IF_LO_FREQUENCY is in Column 4, DDC_LO_FREQUENCY is in Column 5, NCO_FREQUENCY

is in Column 6, and MIXED-DOWN_FREQUENCY is in Column 7. Note that one of the signs in this sum is negative. See documentation of RSR files for further information.

Column 5: DDC_LO_FREQUENCY. Unit=megahertz (MHz). ASCII_Integer (format code I10). Digital Down Converter (DDC) Local Oscillator (LO) Frequency. This specifies the down-conversion applied to the signal in the RSR Digitizer Subassembly (DIG) and DDC. This frequency is needed in order to reconstruct the sky frequency, FSKY, of the data contained in this SFDU: FSKY = RF-IF_LO_FREQUENCY + DDC_LO_FREQUENCY - NCO_FREQUENCY + MIXED-DOWN_FREQUENCY where RF-IF_LO_FREQUENCY is in Column 4, DDC_LO_FREQUENCY is in Column 5, NCO_FREQUENCY is in Column 6, and MIXED-DOWN_FREQUENCY is in Column 7. Note that one of the signs in this sum is negative. See documentation of RSR files for further information.

Column 6: NCO_FREQUENCY. Unit=hertz (Hz). ASCII_Real (format code E20.12). Numerically Controlled Oscillator (NCO) frequency. The frequency over a one millisecond interval beginning at t in msec is evaluated F(t) = F1 + F2*((t+0.5)/1000) + F3*((t+0.5)/1000)**2 where the coefficients F1, F2, and F3 are in columns 61, 62, and 63 of the RSR files. See documentation of RSR files for further information.

Column 7: MIXED-DOWN_FREQUENCY. Unit=hertz (Hz). ASCII_Real (format code E20.12). Mixed-down frequency. The mixed-down frequency is returned from the Fourier transform of the time series of I/Q pairs in the RSR data.

Column 8: ABS_MAX_VALUE. Dimensionless. ASCII_Real (format code E20.12). Absolute value of the Fourier transform of the time series of I/Q pairs in the RSR data at MIXED-DOWN_FREQUENCY. The square of ABS_MAX_VALUE indicates the relative power of the radio signal.

Column 9: IGR_FLAG. Dimensionless. ASCII_Integer (format code I5). Ingress quality flag. Quality flag identifying the data used for analysis of ingress occultation. 0=False, 1=True, 9=Unassigned. Only frequency results with IGR_FLAG=1 are used to generate the corresponding ingress electron density profile.

Column 10: EGR_FLAG. Dimensionless. ASCII_Integer (format code I5). Egress quality

flag. Quality flag identifying the data used for analysis of egress occultation. 0=False, 1=True, 9=Unassigned. Only frequency results with EGR_FLAG=1 are used to generate the corresponding egress electron density profile.

10.1.2 Structure of indn data files

Individual electron density profile data products are stored as comma-separated files and have the extension `.csv`. Each individual electron density profile data product contains eighteen time-ordered columns. The number of rows equals the number of valid electron density measurements. As discussed elsewhere in the text, the number of rows in an individual electron density profile data products is less than the number of rows in the two corresponding frequency data products

Column 1: ETTX. Unit=second. ASCII_Real (format code E20.12). Ephemeris time (seconds past J2000) of transmission of signal from the spacecraft.

Column 2: ETOCC. Unit=second. ASCII_Real (format code E20.12). Ephemeris time (seconds past J2000) of signal closest approach to target body.

Column 3: ETRX. Unit=second. ASCII_Real (format code E20.12). Ephemeris time (seconds past J2000) of reception of signal by DSN station.

Column 4: UTCTX. No unit. ASCII_String (format code A30). UTC time of transmission of signal from the spacecraft.

Column 5: UTCOCC. No unit. ASCII_String (format code A30). UTC time of signal closest approach to target body.

Column 6: UTCRX. No unit. ASCII_String (format code A30). UTC time of reception of signal by DSN station.

Column 7: OCCPTRADIUS. Unit=kilometer. ASCII_Real (format code E20.12). Occultation point radius. The distance between the center of the target body and the signal at the occultation point, or the closest approach to the target body.

Column 8: OCCPTLAT. Unit=degree. ASCII_Real (format code E20.12). Occultation point latitude. Planetocentric latitude of the occultation point. Increases positively north-

ward.

Column 9: OCCPTLON. Unit=degree. ASCII_Real (format code E20.12). Occultation point longitude. Planetocentric longitude of the occultation point. Increases positively eastward.

Column 10: OCCPTSZA. Unit=degree. ASCII_Real (format code E20.12). Occultation point solar zenith angle.

Column 11: OCCPTLST. Unit=hour. ASCII_Real (format code E20.12). Occultation point local true solar time.

Column 12: OCCPTSEP. Unit=degree. ASCII_Real (format code E20.12). Occultation point Sun-Earth-Probe angle, where Probe is the Cassini spacecraft.

Column 13: OCCPTEPS. Unit=degree. ASCII_Real (format code E20.12). Occultation point Earth-Probe-Sun angle, where Probe is the Cassini spacecraft.

Column 14: UNCORRDXDT. Unit=1/(square meter * second). ASCII_Real (format code E20.12). Uncorrected time derivative of the integrated electron column density.

Column 15: CORRDXDT. Unit=1/(square meter * second). ASCII_Real (format code E20.12). Corrected time derivative of the integrated electron column density. As discussed further elsewhere in the text, some UNCORRDXDT time series (from Column 14) required corrections for baseline trends that were measured before or after occultation. Corrections included subtraction of a median value of UNCORRDXDT, subtraction of a linear trend, or replacement of a spurious data point with an interpolation between the previous and next data points. If no correction was applied, then CORRDXDT will equal UNCORRDXDT from Column 14.

Column 16: TEC. Unit=1/(square meter). ASCII_Real (format code E20.12). Total electron content (TEC). TEC is the electron number density integrated along the signal path. The constant of integration was chosen so that TEC is zero at the earliest time.

Column 17: ELECDEN. Unit=1/(cubic centimeter). ASCII_Real (format code E20.12). Electron number density. By construction, ELECDEN is zero at the largest value of OCCPTRADIUS.

Column 18: ELECDENERR. Unit=1/(cubic centimeter). ASCII_Real (format code E20.12). Uncertainty on ELECDEN from Column 17. The uncertainty is calculated as the standard deviation of ELECDEN in the high altitude baseline portion of the observations before or after occultation. Therefore a single value of ELECDENERR applies to all values of ELECDEN in a given individual electron density profile.

Values in columns 1–13 of an individual electron density profile data product are the same for all individual electron density profile data products for a given occultation.

Note that quantities related to total electron content (UNCORRDXDT, CORRDXDT, and TEC) are given in meter-based units (m^{-2} s^{-1} and m^{-2}), whereas quantities related to local electron density (ELECDEN and ELECDENERR) are given in centimeter-based units (cm^{-3}). The data products were generated using SI units (i.e., meter-based). However, long-standing convention in ionospheric physics favors reporting electron densities in units of cm^{-3} (e.g., *Kliore et al.*, 2008, 2011).

10.1.3 Structure of aven data files

Average electron density profile data products are stored as comma-separated files and have the extension `.csv`. Each average electron density profile data product contains fifteen time-ordered columns. The number of rows equals the number of electron density measurements that exist in all of the underlying individual electron density profile data products.

Column 1: ETTX. Unit=second. ASCII_Real (format code E20.12). Ephemeris time (seconds past J2000) of transmission of signal from the spacecraft.

Column 2: ETOCC. Unit=second. ASCII_Real (format code E20.12). Ephemeris time (seconds past J2000) of signal closest approach to target body.

Column 3: ETRX. Unit=second. ASCII_Real (format code E20.12). Ephemeris time (seconds past J2000) of reception of signal by DSN station.

Column 4: UTCTX. No unit. ASCII_String (format code A30). UTC time of transmission of signal from the spacecraft.

Column 5: UTCOCC. No unit. ASCII_String (format code A30). UTC time of signal

closest approach to target body.

Column 6: UTCRX. No unit. ASCII_String (format code A30). UTC time of reception of signal by DSN station.

Column 7: OCCPTRADIUS. Unit=kilometer. ASCII_Real (format code E20.12). Occultation point radius. The distance between the center of the target body and the signal at the occultation point, or the closest approach to the target body.

Column 8: OCCPTLAT. Unit=degree. ASCII_Real (format code E20.12). Occultation point latitude. Planetocentric latitude of the occultation point. Increases positively northward.

Column 9: OCCPTLON. Unit=degree. ASCII_Real (format code E20.12). Occultation point longitude. Planetocentric longitude of the occultation point. Increases positively eastward.

Column 10: OCCPTSZA. Unit=degree. ASCII_Real (format code E20.12). Occultation point solar zenith angle.

Column 11: OCCPTLST. Unit=hour. ASCII_Real (format code E20.12). Occultation point local true solar time.

Column 12: OCCPTSEP. Unit=degree. ASCII_Real (format code E20.12). Occultation point Sun-Earth-Probe angle, where Probe is the Cassini spacecraft.

Column 13: OCCPTEPS. Unit=degree. ASCII_Real (format code E20.12). Occultation point Earth-Probe-Sun angle, where Probe is the Cassini spacecraft.

Column 14: AVGELECDEN. Unit=1/(cubic centimeter). ASCII_Real (format code E20.12). Averaged electron number density. AVGELECDEN has uncertainty AVGELECDENERR, where AVGELECDEN and AVGELECDENERR satisfy AVGELECDEN / AVGELECDENERR $= \Sigma$ ELECDEN$_i$ / ELECDENERR$_i^2$ and 1 / AVGELECDENERR$^2 = \Sigma$ 1 / ELECDENERR$_i^2$. Here ELECDEN$_i$ are densities from individual profiles and ELECDENERR$_i$ are the corresponding uncertainties.

Column 15: AVGELECDENERR. Unit=1/(cubic centimeter). ASCII_Real (format code E20.12). Uncertainty on AVGELECDEN from Column 14. Value calculated as described

for AVGELECDEN from Column 14. A single value of AVGELECDENERR applies to all values of AVGELECDEN in a given average electron density profile.

Values in columns 1-13 of an average electron density profile data product match values in columns 1-13 of the associated individual electron density profile data products.

Note that quantities related to local electron density (AVGELECDEN and AVGELECDENERR) are given in centimeter-based units (cm^{-3}). The data products were generated using SI units (i.e., meter-based). However, long-standing convention in ionospheric physics favors reporting electron densities in units of cm^{-3} (e.g., *Kliore et al.*, 2008, 2011).

10.1.4 Structure of summ data files

Summary table data products are stored as comma-separated files and have the extension `.csv`. Each summary table data product contains nine time-ordered columns. The number of rows equals the number of average electron density profile data products for the specified target object.

Column 1: OBSERVATION. No unit. ASCII_String (format code A10). Flyby and observation identifier. The first four characters identify the flyby (e.g., "T014") and the final character identifies ingress ("N") or egress ("X").

Column 2: UTCOCC. No unit. ASCII_String (format code A30). UTC time of signal closest approach to target body.

Column 3: OCCPTLAT. Unit=degree. ASCII_Real (format code E20.12). Occultation point latitude. Planetocentric latitude of the occultation point. Increases positively northward.

Column 4: OCCPTLON. Unit=degree. ASCII_Real (format code E20.12). Occultation point longitude. Planetocentric longitude of the occultation point. Increases positively eastward.

Column 5: OCCPTSZA. Unit=degree. ASCII_Real (format code E20.12). Occultation point solar zenith angle.

Column 6: OCCPTLST. Unit=hour. ASCII_Real (format code E20.12). Occultation

point local true solar time.

Column 7: OCCPTSEP. Unit=degree. ASCII_Real (format code E20.12). Occultation point Sun-Earth-Probe angle, where Probe is the Cassini spacecraft.

Column 8: OCCPTEPS. Unit=degree. ASCII_Real (format code E20.12). Occultation point Earth-Probe-Sun angle, where Probe is the Cassini spacecraft.

Column 9: AVGELECDENERR. Unit=1/(cubic centimeter). ASCII_Real (format code E20.12). Uncertainty on AVGELECDEN.

Each row in this summary file contains values that can be found in a single row of the relevant average electron density profile data product. For Titan, this is the row for which OCCPTRADIUS is closest to 2575 km + 1200 km = 3775 km. This radial distance, which is representative of the location of maximum ionospheric electron density, was chosen for consistency with *Kliore et al.* (2008).

Note that quantities related to local electron density (AVGELECDENERR) are given in centimeter-based units (cm^{-3}). The data products were generated using SI units (i.e., meter-based). However, long-standing convention in ionospheric physics favors reporting electron densities in units of cm^{-3} (e.g., *Kliore et al.*, 2008, 2011).

10.2 PDS labels

PDS labels are ASCII text files written in the eXtensible Markup Language (XML). All product labels are detached from the digital files (if any) containing the data objects they describe (except Product_Bundle). There is one label for every product. Each product, however, may contain one or more data objects. The data objects of a given product may all reside in a single file, or they may be stored in multiple separate files. PDS4 label files must end with the file extension "`.xml`".

For this archive, PDS labels will conform to the PDS master schema based upon version 1.8.0.0 of the PDS information model for structure and version 1.8.0.0 of the PDS schematron for content. By use of an XML editor these documents may be used to validate the structure and content of the product labels. A list of the XML documents associated with this archive

is included in the XML_Schema collection section for each bundle.

11 Naming conventions

This section describes the naming conventions used for the basic product filenames.

11.1 Naming convention for freq products

A sample filename for a frequency data product is:

`s20tioc2006140_1317nnnk55rv_1n2_freq_v01_r00.csv`

The file naming convention is:

`sssttaayyyyddd_hhmmxuudrrpq_rcs_freq_vxx_rxx.csv`

where:

`sss`: Sequence or orbit number. `c26-c32` for Quiet Cruise, `c33-c41` for Space Science, `c42-c44` for Approach Science, and ≥`s00` for Tour.

`tt`: Target. `ti` for Titan, `sa` for Saturn, `sr` for Saturn and rings, `en` for Enceladus, and `r[i,a,b,c,d,e,f,g,h,1,2,...]` for rings.

`aa`: Activity or experiment ID. `oc` for general occultation experiment, `oi` for ingress occultation experiment, `oe` for egress occultation experiment.

`yyyy`: Year corresponding to RSR start time (ground-received time, UTC).

`ddd`: Day of year corresponding to RSR start time (ground-received time, UTC).

`hhmm`: Hours and minutes corresponding to RSR start time (ground-received time, UTC).

`xuu`: Uplink band(s) and transmitting station(s). Bands may be "`s`", "`x`", or "`k`" for S-band, X-band, and Ka-band, respectively. Transmitting stations are the standard two-digit identifiers of the Deep Space Network Station (DSS). These are listed in Deep Space Network document 820-013, OPS-6-3, and the allowed values include 14, 15, 25, 43, 45, 54, and 63. "`nnn`" means 1-way (no uplink).

`drr`: Downlink band(s) and receiving station(s). Bands may be "`s`", "`x`", or "`k`" for S-band, X-band, and Ka-band, respectively. Receiving stations are the standard two-digit

identifiers of the Deep Space Network Station (DSS). These are listed in Deep Space Network document 820-013, OPS-6-3, and the allowed values include 14, 15, 25, 43, 45, 54, and 63.

`p`: Polarization. `r` for right circulation, `l` for left circular.

`q`: Receiver type. `d` for RSR, `v` for VSR (VLBI science receiver), or `w` for WVSR (Wideband VLBI science receiver).

`rcs`: RSR + channel + subchannel (e.g., `1a1`, `1a2`, `1b3`, `3a1`, etc.)

`freq`: indicates that this is a frequency data product

`vxx`: identifies the major component `xx` of the version number of this product

`rxx`: identifies the minor component `xx` of the version number of this product

`csv`: indicates that this data product is a comma-separated file

In order to facilitate traceability from RSR data file to associated frequency data product, the first 31 characters of the filename for a frequency data product mimic the naming convention of the associated RSR file. Hence frequency data product

`sssttaayyyyddd_hhmmxuudrrpq_rcs_freq_vxx_rxx.csv`

was derived from RSR file

`sssttaayyyyddd_hhmmxuudrrpq.rcs`

11.2 Naming convention for indn products

A sample filename for an individual electron density profile data product is:

`s20tioc2006140_1317_n_sx_63_titan_edp_v01_r00.csv`

The file naming convention is:

`sssttaayyyyddd_hhmm_t_bb_nn_ooooo_edp_vxx_rxx.csv`

where:

`sss`: Sequence or orbit number. `c26-c32` for Quiet Cruise, `c33-c41` for Space Science, `c42-c44` for Approach Science, and $\geq$`s00` for Tour.

`tt`: Target. `ti` for Titan, `sa` for Saturn, `sr` for Saturn and rings, `en` for Enceladus, and `r[i,a,b,c,d,e,f,g,h,1,2,...]` for rings.

aa: Activity or experiment ID. oc for general occultation experiment, oi for ingress occultation experiment, oe for egress occultation experiment.

yyyy: Year corresponding to RSR start time.

ddd: Day of year corresponding to RSR start time.

hhmm: Hours and minutes corresponding to RSR start time. Use of the RSR start time, not the time of the earliest electron density measurement in the data file, ensures traceability to the underlying frequency data products and RSR data files.

t: Ingress or egress identifier. n for ingress, x for egress.

bb: Combination of bands, either sx (S-band and X-band) or xk (X-band and Ka-band).

nn: DSN station identifier.

ooooo: Target name. First five characters in the name of the target body (e.g., titan, satur).

edp: indicates that this is an electron density data product.

vxx: identifies the major component xx of the version number of this product

rxx: identifies the minor component xx of the version number of this product

csv: indicates that this data product is a comma-separated file.

In order to facilitate traceability from frequency data products to the associated individual electron density profile data product, the first 19 characters of the filename of an individual electron density profile data product mimics the naming convention of the associated frequency data products. Hence individual electron density profile data product

sssttaayyyyddd_hhmm_t_bb_nn_ooooo_edp_vxx_rxx.csv

was derived from frequency data product

sssttaayyyyddd_hhmmxuudrrpq_rcs_freq_vxx.csv

11.3 Naming convention for aven products

A sample filename for an average electron density profile data product is:

s20_t014n_titan_edp_v01_r00.csv

The file naming convention is:

`sss_fffff_ooooo_edp_vxx_rxx.csv`

where:

`sss`: Sequence or orbit number. `c26-c32` for Quiet Cruise, `c33-c41` for Space Science, `c42-c44` for Approach Science, and $\geq$`s00` for Tour.

`fffff`: Flyby and observation identifier. The first four characters identify the flyby (e.g., "`t014`") and the final character identifies ingress ("`n`") or egress ("`x`").

`ooooo`: Target name. First five characters in the name of the target body (e.g., `titan`, `satur`).

`edp`: indicates that this is an electron density data product.

`vxx`: identifies the major component `xx` of the version number of this product

`rxx`: identifies the minor component `xx` of the version number of this product

`csv`: indicates that this data product is a comma-separated file.

11.4 Naming convention for summ products

A sample filename for a summary table data product is:

`titan_summary_table_v01_r00.csv`

The file naming convention is:

`ooooo_summary_table_vxx_rxx.csv`

where:

`ooooo`: Target name. First five characters in the name of the target body (e.g., `titan`, `satur`).

`vxx`: identifies the major component `xx` of the version number of this product

`rxx`: identifies the minor component `xx` of the version number of this product

`csv`: indicates that this data product is a comma-separated file.

12 Derivation of $\Omega(r) = N(r)\sqrt{2\pi r H}$

$\Omega(X)$ is related to $N(r)$ via:

$$\Omega(X) = 2\int_{r=X}^{r=\infty} \frac{Nrdr}{\sqrt{r^2 - X^2}} \tag{7}$$

We now derive the result that $\Omega(r) = N(r)\sqrt{2\pi rH}$ for the special case where N decreases exponentially with increasing r with scale height H. We assume $N(r) = N_0 \exp(-r/H)$, which leads to:

$$\Omega(X) = 2\int_{r=X}^{r=\infty} N_0 \exp(-r/H)\, r \left(r^2 - X^2\right)^{-1/2} dr \tag{8}$$

Let $x = r/X$.

$$\Omega(X) = 2N_0 \int_{x=1}^{x=\infty} \exp(-xX/H)\, xX \left(x^2X^2 - X^2\right)^{-1/2} Xdx \tag{9}$$

$$\Omega(X) = 2N_0 \int_{x=1}^{x=\infty} \exp(-xX/H)\, x \left(x^2 - 1\right)^{-1/2} Xdx \tag{10}$$

Let $z = X/H$, where the symbol z is adopted for consistency with *Arfken and Weber* (1995) and should not be confused with altitude z used elsewhere in this document.

$$\Omega(X) = 2N_0 X \int_{x=1}^{x=\infty} \exp(-zx)\, x \left(x^2 - 1\right)^{-1/2} dx \tag{11}$$

To solve this integral, we introduce the modified Bessel function of the second kind of order 1, $K_1(z)$, which satisfies (*Arfken and Weber*, 1995, Equation 11.122):

$$K_1(z) = \frac{\pi^{1/2}}{\left(1 - \frac{1}{2}\right)!} \left(\frac{z}{2}\right)^1 \int_{x=1}^{x=\infty} \exp(-zx) \left(x^2 - 1\right)^{(1-1/2)} dx \tag{12}$$

As $(n-1)! = \Gamma(n)$, we have $\left(1 - \frac{1}{2}\right)! = (0.5)! = \Gamma(1.5) = 0.5\,\pi^{1/2}$. Hence Equation 12 becomes:

$$K_1(z) = z \int_{x=1}^{x=\infty} \exp(-zx) \left(x^2 - 1\right)^{1/2} dx \tag{13}$$

Rearranging:

$$\frac{K_1(z)}{z} = \int_{x=1}^{x=\infty} \exp(-zx) \left(x^2 - 1\right)^{1/2} dx \tag{14}$$

Integrating by parts, we have:

$$\frac{K_1(z)}{z} = \left[\left(\frac{-1}{z}\right) \exp(-zx) \left(x^2 - 1\right)^{1/2}\right]_{x=1}^{x=\infty} - \int_{x=1}^{x=\infty} \left(\frac{-1}{z}\right) \exp(-zx)\, x \left(x^2 - 1\right)^{-1/2} dx \tag{15}$$

The first term on the right hand side is zero at each limit (assuming $z > 0$, which is appropriate here). This gives:

$$K_1(z) = \int_{x=1}^{x=\infty} \exp(-zx)\, x \left(x^2 - 1\right)^{-1/2} dx \tag{16}$$

Combining Equations 11 and 16 gives:

$$\Omega(X) = (2N_0 X)\,(K_1(z)) \tag{17}$$

In the limit that $z \gg 1$, $K_1(z) = \sqrt{\frac{\pi}{2z}} \exp(-z)$ (*Arfken and Weber*, 1995, Equation 11.127). This limit applies here because $z = X/H$, X is on the order of the planetary radius, and $X \gg H$. Hence:

$$\Omega(X) = (2N_0 X) \left(\sqrt{\frac{\pi}{2z}} \exp(-z)\right) \tag{18}$$

Replacing z with X/H gives:

$$\Omega(X) = \sqrt{2\pi X H} N_0 \exp(-X/H) \tag{19}$$

Replacing X with the familiar r and noting that $N(r) = N_0 \exp(-r/H)$ yields the desired result:

$$\Omega(r) = N(r)\sqrt{2\pi r H} \tag{20}$$

13 Acknowledgements

This work was supported, in part, by NASA award NNX15AI87G. This research made use of the Shared Computing Cluster administered by Boston University's Research Computing Services at the Massachusetts Green High Performance Computing Center. We thank Dick French, Andy Nagy, and Paul Schinder of the Cassini RSS team for their advice and encouragement.

14 References

References

Ågren, K., J.-E. Wahlund, P. Garnier, R. Modolo, J. Cui, M. Galand, and I. Müller-Wodarg (2009), On the ionospheric structure of Titan, *Planet. Space Sci.*, *57*, 1821–1827, doi: 10.1016/j.pss.2009.04.012.

Arfken, G. B., and H. J. Weber (1995), *Mathematical methods for physicists, fourth edition*, Academic Press, San Deigo.

Bird, M. K., R. Dutta-Roy, S. W. Asmar, and T. A. Rebold (1997), Detection of Titan's Ionosphere from Voyager 1 Radio Occultation Observations, *Icarus*, *130*, 426–436, doi: 10.1006/icar.1997.5831.

Bocanegra-Bahamón, T. M., G. Molera Calvés, L. I. Gurvits, D. A. Duev, S. V. Pogrebenko, G. Cimò, D. Dirkx, and P. Rosenblatt (2018), Planetary Radio Interferometry and Doppler Experiment (PRIDE) technique: A test case of the Mars Express Phobos Flyby. II. Doppler tracking: Formulation of observed and computed values, and noise budget, *Astron. Astrophys.*, *609*, A59, doi:10.1051/0004-6361/201731524.

Coates, A. J., J.-E. Wahlund, K. Ågren, N. Edberg, J. Cui, A. Wellbrock, and K. Szego (2011), Recent Results from Titan's Ionosphere, *Space Sci. Rev.*, *162*, 85–111, doi: 10.1007/s11214-011-9826-4.

Cravens, T. E., R. V. Yelle, J.-E. Wahlund, D. E. Shemansky, and A. F. Nagy (2010), Composition and Structure of the Ionosphere and Thermosphere, in *Titan from Cassini-Huygens*, edited by R. H. Brown, J.-P. Lebreton, and J. H. Waite, pp. 259–296, doi: 10.1007/978-1-4020-9215-2_11.

Dalba, P. A., and P. Withers (2019), Cassini Radio Occultation Observations of Titan's Ionosphere: The Complete Set of Electron Density Profiles, *J. Geophys. Res.*, *124*(1), 643–660, doi:10.1029/2018JA025693.

Del Genio, A. D., R. K. Achterberg, K. H. Baines, F. M. Flasar, P. L. Read, A. Sanchez-Lavega, and A. P. Showman (2009), Saturn Atmospheric Structure and Dynamics, in *Saturn from Cassini-Huygens*, edited by M. K. Dougherty, L. W. Esposito, and S. M. Krimigis, pp. 113–160, doi:10.1007/978-1-4020-9217-6_6.

Edberg, N. J. T., D. J. Andrews, C. Bertucci, D. A. Gurnett, M. K. G. Holmberg, C. M. Jackman, W. S. Kurth, J. D. Menietti, H. J. Opgenoorth, O. Shebanits, E. Vigren, and J.-E. Wahlund (2015), Effects of Saturn's magnetospheric dynamics on Titan's ionosphere, *J. Geophys. Res.*, *120*, 8884–8898, doi:10.1002/2015JA021373.

Eshleman, V. R. (1973), The radio occultation method for the study of planetary atmospheres, *Planet. Space Sci.*, *21*, 1521–1531.

Fjeldbo, G., A. J. Kliore, and V. R. Eshleman (1971), The neutral atmosphere of Venus as studied with the Mariner V radio occultation experiments, *Astron. J.*, *76*, 123–140.

Flasar, F. M., K. H. Baines, M. K. Bird, T. Tokano, and R. A. West (2010), Atmospheric Dynamics and Meteorology, in *Titan from Cassini-Huygens*, edited by R. H. Brown, J.-P. Lebreton, and J. H. Waite, pp. 323–352, doi:10.1007/978-1-4020-9215-2_13.

Hinson, D. P., R. A. Simpson, J. D. Twicken, G. L. Tyler, and F. M. Flasar (1999), Initial results from radio occultation measurements with Mars Global Surveyor, *J. Geophys. Res.*, *104*, 26,997–27,012.

Karayel, E. T., and D. P. Hinson (1997), Sub-Fresnel-scale vertical resolution in atmospheric profiles from radio occultation, *Radio Sci.*, *32*, 411–424, doi:10.1029/96RS03212.

Kliore, A., and E. Barbinis (2010), Cassini Radio Occultation Profiles of the Titan

Ionosphere from Publications up to September 2008, *NASA Planetary Data System, USA_NASA_JPL_CORS_1001, CO-SSA-RSS-5-EDP1-V1.0*.

Kliore, A., J. Armstrong, F. Flasar, R. French, E. Marouf, A. Nagy, N. Rappaport, C. McGhee, P. Schinder, A. Anabtawi, S. Asmar, E. Barbinis, D. Fleischman, G. Goltz, R. Aguilar, and D. Rochblatt (2006), Cassini Radio Occultation by Enceladus Plume, *AGU Fall Meeting Abstracts*, P13B-0177.

Kliore, A., E. Marouf, A. Nagy, S. Asmar, F. M. Flasar, A. Anabtawi, E. Barbinis, D. Fleischman, D. Kahan, and J. Klose (2010a), The plasma environment of Enceladue from the Cassini plume radio occultation, in *38th COSPAR Scientific Assembly*, *COSPAR Meeting*, vol. 38, p. 6.

Kliore, A., A. Nagy, and E. Marouf (2010b), The Plasma Cloud of Enceladus, in *European Planetary Science Congress 2010*, p. 113.

Kliore, A. J., J. D. Anderson, J. W. Armstrong, S. W. Asmar, C. L. Hamilton, N. J. Rappaport, H. D. Wahlquist, R. Ambrosini, F. M. Flasar, R. G. French, L. Iess, E. A. Marouf, and A. F. Nagy (2004), Cassini Radio Science, *Space Sci. Rev.*, *115*, 1–70, doi: 10.1007/s11214-004-1436-y.

Kliore, A. J., A. F. Nagy, E. A. Marouf, R. G. French, F. M. Flasar, N. J. Rappaport, A. Anabttawi, S. W. Asmar, D. S. Kahann, E. Barbinis, G. L. Goltz, D. U. Fleischman, and D. J. Rochblatt (2008), First results from the Cassini radio occultations of the Titan ionosphere, *J. Geophys. Res.*, *113*, A09317, doi:10.1029/2007JA012965.

Kliore, A. J., A. F. Nagy, and E. A. Marouf (2010c), The Nature of the Enceladus Plasma Cloud From the Cassini Plume Radio Occultation, *AGU Fall Meeting Abstracts*, P33A-1568.

Kliore, A. J., A. F. Nagy, T. E. Cravens, M. S. Richard, and A. M. Rymer (2011), Unusual electron density profiles observed by Cassini radio occultations in Titan's ionosphere: Ef-

fects of enhanced magnetospheric electron precipitation?, *J. Geophys. Res.*, *116*, A11318, doi:10.1029/2011JA016694.

Kliore, A. J., A. F. Nagy, T. Cravens, and A. Anabtawi (2013), The Cassini Radio Science Observations of the Enceladus Plasma Cloud, *AGU Fall Meeting Abstracts*, P53B-1853.

Moore, L., A. F. Nagy, A. J. Kliore, I. Müller-Wodarg, J. D. Richardson, and M. Mendillo (2006), Cassini radio occultations of Saturn's ionosphere: Model comparisons using a constant water flux, *Geophys. Res. Lett.*, *33*, L22202, doi:10.1029/2006GL027375.

Nagy, A. F., A. J. Kliore, E. Marouf, R. French, M. Flasar, N. J. Rappaport, A. Anabtawi, S. W. Asmar, D. Johnston, E. Barbinis, G. Goltz, and D. Fleischman (2006), First results from the ionospheric radio occultations of Saturn by the Cassini spacecraft, *J. Geophys. Res.*, *111*, A06310, doi:10.1029/2005JA011519.

Nagy, A. F., A. J. Kliore, M. Mendillo, S. Miller, L. Moore, J. I. Moses, I. Müller-Wodarg, and D. Shemansky (2009), Upper Atmosphere and Ionosphere of Saturn, in *Saturn from Cassini-Huygens*, edited by M. K. Dougherty, L. W. Esposito, and S. M. Krimigis, pp. 181–201, doi:10.1007/978-1-4020-9217-6_8.

Pätzold, M., and thirty colleagues (2009), *MaRS: Mars Express Radio Science Experiment*, pp. 217–245, ESA SP-1291: Mars Express: the Scientific Investigations, available online at http://sci.esa.int/science-e/www/object/index.cfm?fobjectid=47218.

Pätzold, M., F. M. Neubauer, L. Carone, A. Hagermann, C. Stanzel, B. Häusler, S. Remus, J. Selle, D. Hagl, D. P. Hinson, R. A. Simpson, G. L. Tyler, S. W. Asmar, W. I. Axford, T. Hagfors, J.-P. Barriot, J.-C. Cerisier, T. Imamura, K.-I. Oyama, P. Janle, G. Kirchengast, and V. Dehant (2004), *MaRS: Mars Express Orbiter Radio Science*, pp. 141–163, ESA SP-1240: Mars Express: the Scientific Payload, available online at http://sci.esa.int/science-e/www/object/index.cfm?fobjectid=34885.

Press, W. H., B. P. Flannery, S. A. Teukolsky, and W. T. Vetterling (1988), *Numerical Recipes in C*, Cambridge Univ. Press, New York.

Quémerais, E., J.-L. Bertaux, O. Korablev, E. Dimarellis, C. Cot, B. R. Sandel, and D. Fussen (2006), Stellar occultations observed by SPICAM on Mars Express, *J. Geophys. Res.*, *111*, E09S04, doi:10.1029/2005JE002604.

Schinder, P. J., F. M. Flasar, E. A. Marouf, R. G. French, C. A. McGhee, A. J. Kliore, N. J. Rappaport, E. Barbinis, D. Fleischman, and A. Anabtawi (2011a), Saturn's equatorial oscillation: Evidence of descending thermal structure from Cassini radio occultations, *Geophys. Res. Lett*, *38*, L08205, doi:10.1029/2011GL047191.

Schinder, P. J., F. M. Flasar, E. A. Marouf, R. G. French, C. A. McGhee, A. J. Kliore, N. J. Rappaport, E. Barbinis, D. Fleischman, and A. Anabtawi (2011b), The structure of Titan's atmosphere from Cassini radio occultations, *Icarus*, *215*, 460–474, doi:10.1016/j.icarus.2011.07.030.

Schinder, P. J., F. M. Flasar, E. A. Marouf, R. G. French, C. A. McGhee, A. J. Kliore, N. J. Rappaport, E. Barbinis, D. Fleischman, and A. Anabtawi (2012), The structure of Titan's atmosphere from Cassini radio occultations: Occultations from the Prime and Equinox missions, *Icarus*, *221*, 1020–1031, doi:10.1016/j.icarus.2012.10.021.

Schinder, P. J., F. M. Flasar, E. A. Marouf, R. G. French, A. Anabtawi, E. Barbinis, and A. J. Kliore (2015), A numerical technique for two-way radio occultations by oblate axisymmetric atmospheres with zonal winds, *Radio Science*, *50*, 712–727, doi:10.1002/2015RS005690.

Strobel, D. F., S. K. Atreya, B. Bézard, F. Ferri, F. M. Flasar, M. Fulchignoni, E. Lellouch, and I. Müller-Wodarg (2010), Atmospheric Structure and Composition, in *Titan from Cassini-Huygens*, edited by R. H. Brown, J.-P. Lebreton, and J. H. Waite, pp. 235–258, doi:10.1007/978-1-4020-9215-2_10.

Tokano, T. (2014), Non-uniform global methane distribution in Titan's troposphere evidenced by Cassini radio occultations, *Icarus*, *231*, 1–12, doi:10.1016/j.icarus.2013.11.030.

Withers, P. (2010), Prediction of uncertainties in atmospheric properties measured by radio occultation experiments, *Adv. Space Res.*, *46*, 58–73, doi:10.1016/j.asr.2010.03.004.

Withers, P., L. Moore, K. Cahoy, and I. Beerer (2014), How to process radio occultation data: 1. From time series of frequency residuals to vertical profiles of atmospheric and ionospheric properties, *Planet. Space Sci.*, *101*, 77–88, doi:10.1016/j.pss.2014.06.011.

15 Tables

Table 1: Summary of Titan electron density profiles

Occ.	Date (UTC)	Lat. (°N)	Lon. (°E)	SZA[a] (degrees)	LST[b] (hrs)	SEP[c] angle (degrees)	EPS[d] angle (degrees)	Ram angle[e] (degrees)	σ_N (cm^{-3})
T012N	19 Mar 2006[f]	-15	162	95.0	5.3	126	5	73	120
T012X	19 Mar 2006[f]	-35	2	87.5	18.7	126	5	88	152
T014N	20 May 2006	-20	-170	95.8	5.1	67	6	100	180
T014X	20 May 2006	-21	25	85.8	18.1	67	6	66	238
T027N	26 Mar 2007	-75	-138	92.2	0.6	134	5	94	108
T027X	26 Mar 2007	60	90	90.0	7.7	134	5	60	102
T031N	28 May 2007	-75	-33	92.3	23.1	72	6	98	212
T031X	28 May 2007	74	126	88.2	9.8	72	6	77	216
T046N	03 Nov 2008	-33	-60	92.3	18.4	53	5	137	99
T046X	03 Nov 2008	33	119	87.8	6.4	53	5	43	113
T052N	04 Apr 2009	81	97	88.1	16.3	152	3	81	129
T052X	04 Apr 2009	-25	121	88.4	17.9	152	3	39	111
T057N	22 Jun 2009	76	-46	88.6	6.5	75	6	100	488
T101N	17 May 2014	-53	-60	90.7	8.0	172	1	122	149
T101X	17 May 2014	68	175	89.6	23.7	172	1	88	185
T102N	18 Jun 2014	-64	-39	92.0	9.4	140	4	106	169
T102X	18 Jun 2014	64	138	87.9	21.2	140	4	73	150
T117N	16 Feb 2016	-37	38	93.4	16.9	73	5	61	858
T117X	17 Feb 2016	53	100	92.7	21.1	73	5	53	408
T119X	06 May 2016	51	-157	88.6	3.8	152	3	104	204

Dates and locations based on ray path with closest approach distance of 3775 km. Horizontal lines separate profiles first reported in *Kliore et al.* (2008) and previously archived on the PDS (T012-T031), profiles first reported in *Kliore et al.* (2011) (T046–T057), and profiles first reported in this archive (T101–T119).

a — Solar zenith angle.

b — Local solar time.

c — Sun-Earth-Probe angle, where "Probe" is Cassini.

d — Earth-Probe-Sun angle, where "Probe" is Cassini.

e — Ram angle, defined as angular separation between the occultation location and the magnetospheric ram point at 0°N, 90°E.

f — Listed as 20 March 2006 in *Kliore et al.* (2008) and *Kliore et al.* (2011) in an apparent typographical error.

16 Figures

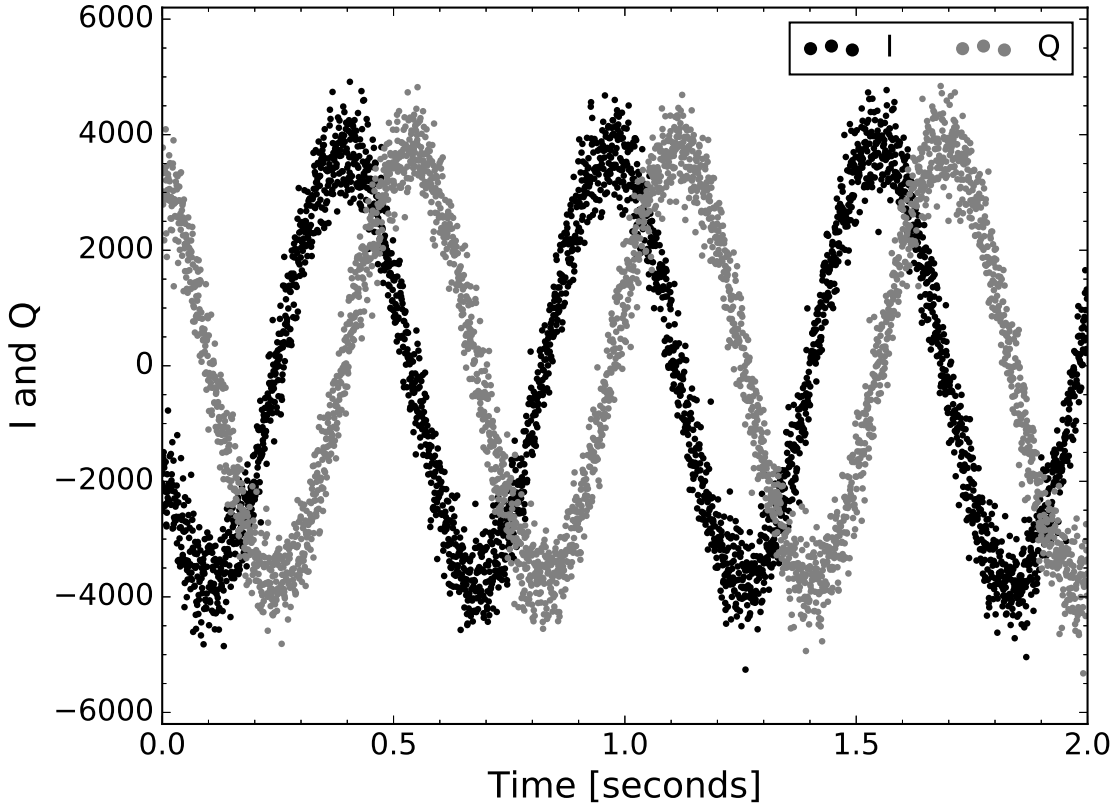

Figure 1: Two seconds of I/Q data for X-band data received at DSS-14, a 70m antenna at Goldstone, during the T012X occultation.

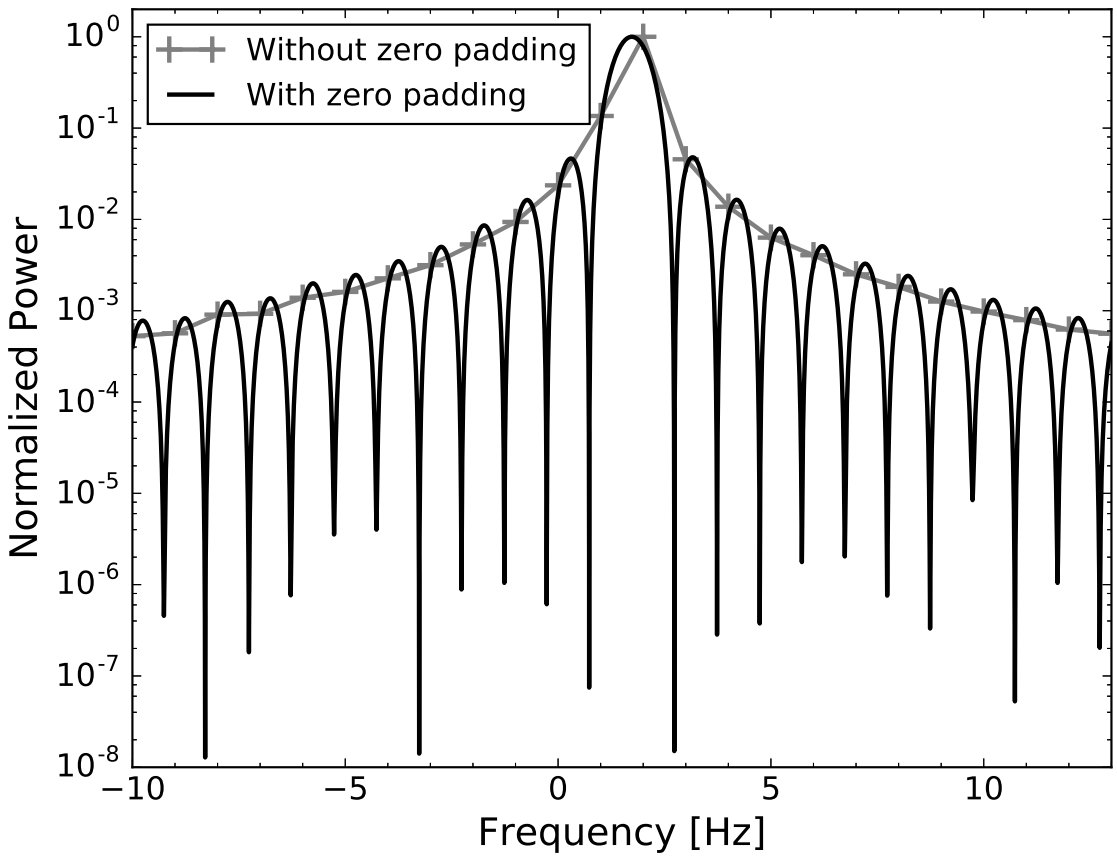

Figure 2: Power spectrum of the first second of I/Q data shown in Figure 1. Results with zero padding are shown by the black curve. Results without zero padding are shown by the grey curve with symbols plotted at each data point.

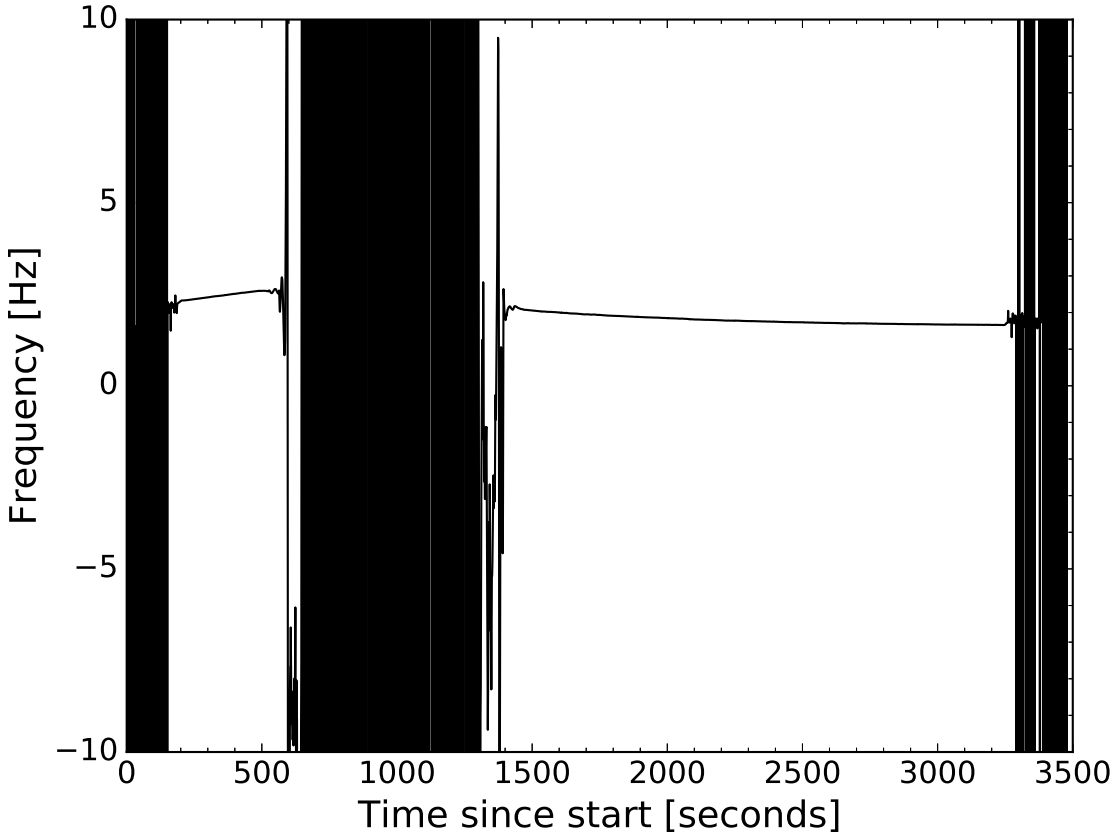

Figure 3: Full time series of mixed-down frequency measurements from X-band observations at DSS-14 during occultation T012.

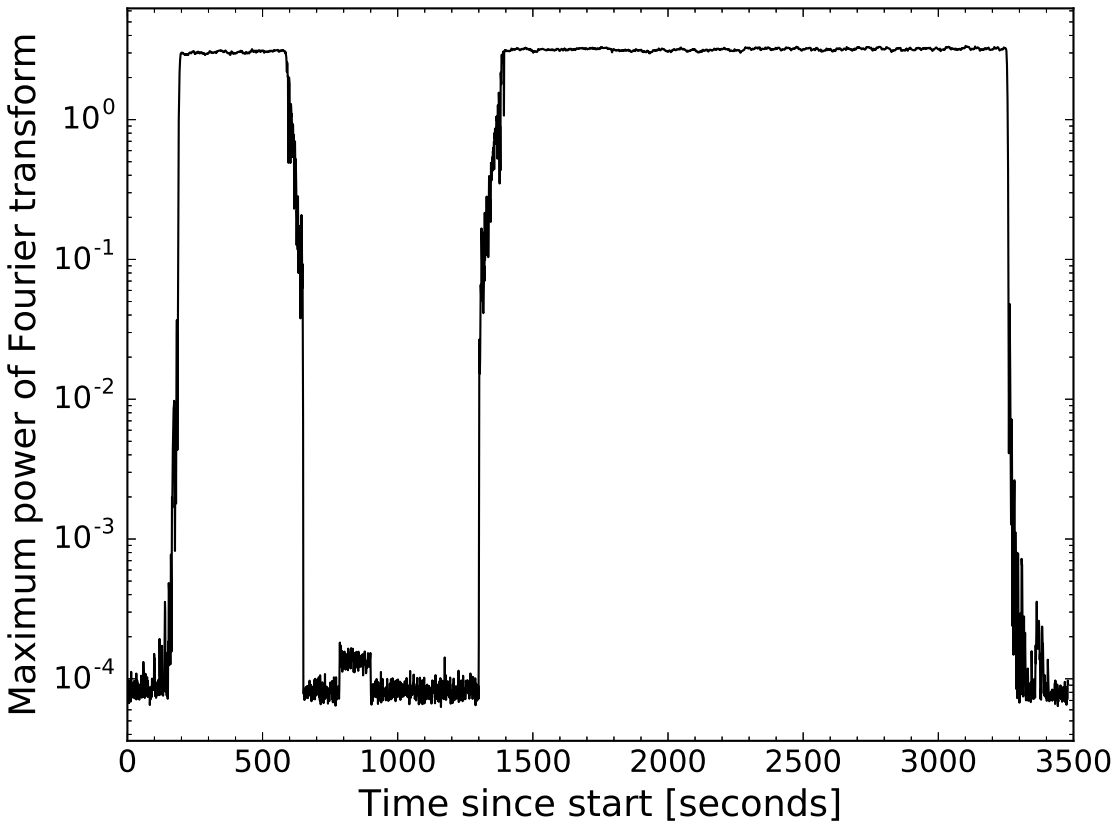

Figure 4: Full time series of the square of the absolute value of the Fourier transform at the inferred frequency from X-band observations at DSS-14 during occultation T012.

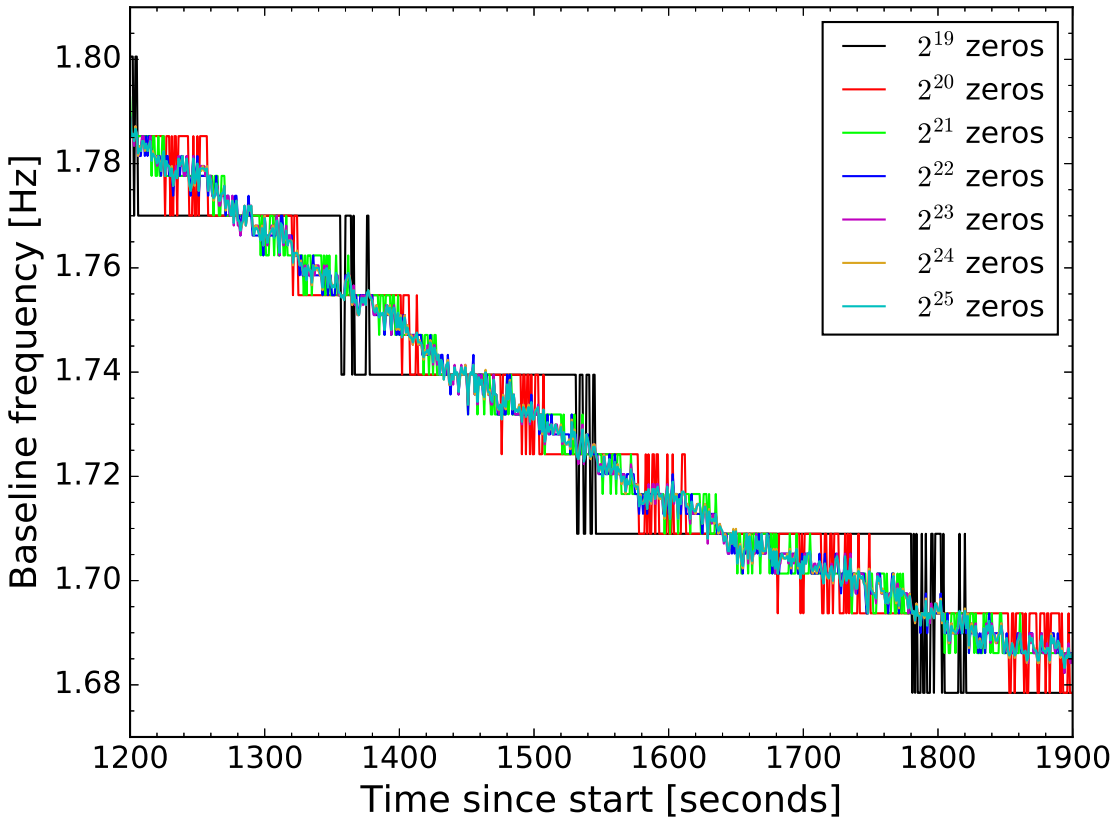

Figure 5: Time series of mixed-down frequency measurements from X-band observations at DSS-14 during occultation T012. Data from after the egress occultation are shown, so data should not be affected by Titan's environment. Multiple versions of the frequencies are shown, with different zero padding lengths indicated by line color.

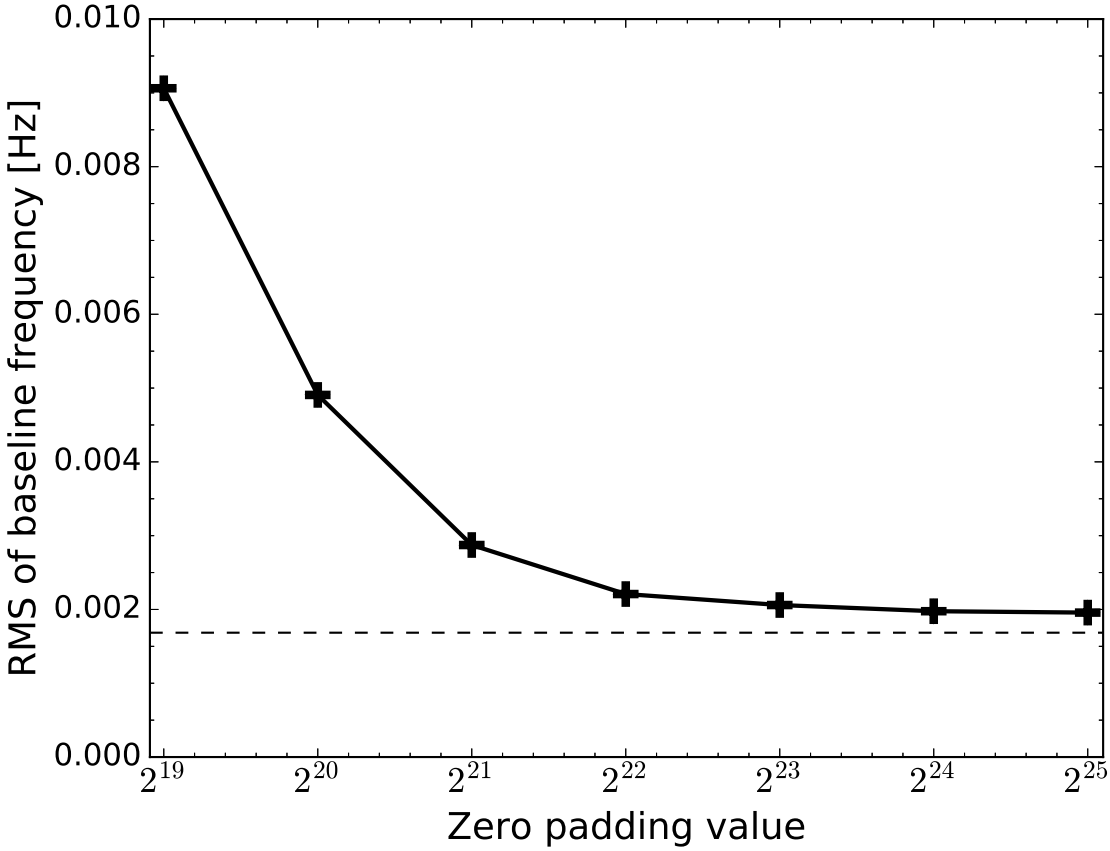

Figure 6: Root-mean-square residuals between frequency measurements of Figure 5 and quadratic fit. Dependence of residuals on length of zero padding is shown. Horizontal line shows accuracy limit of 1.6 mHz for an 8.4 GHz (X-band) signal generated by the Cassini USO, which has Allan deviation of 2×10^{-13} at a time interval of one second (*Kliore et al.*, 2004).

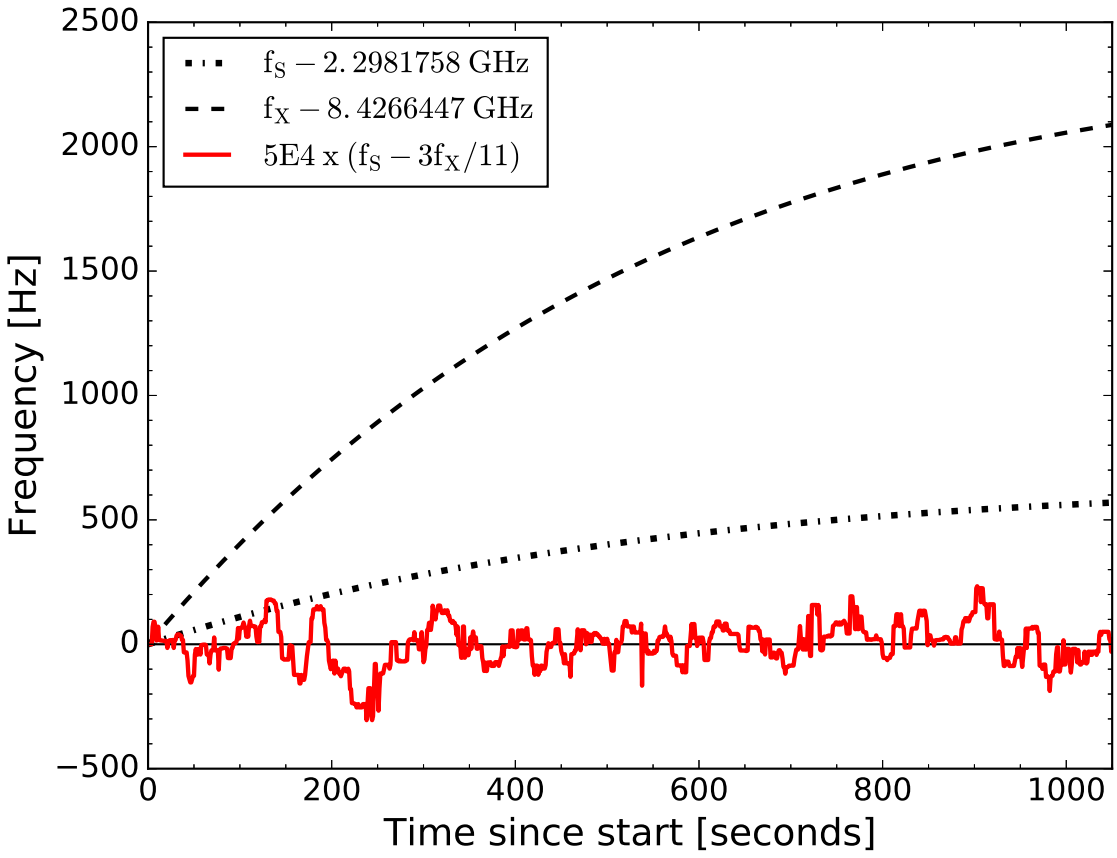

Figure 7: Time series of f_S, f_X, and $f_S - 3f_X/11$ from observations at DSS-14 during occultation T012X. The horizontal line indicates zero. Deviations of $f_S - 3f_X/11$ from zero at 200 seconds indicate the ionosphere. The results for $f_S - 3f_X/11$ show 10-second averaged values for clarity.

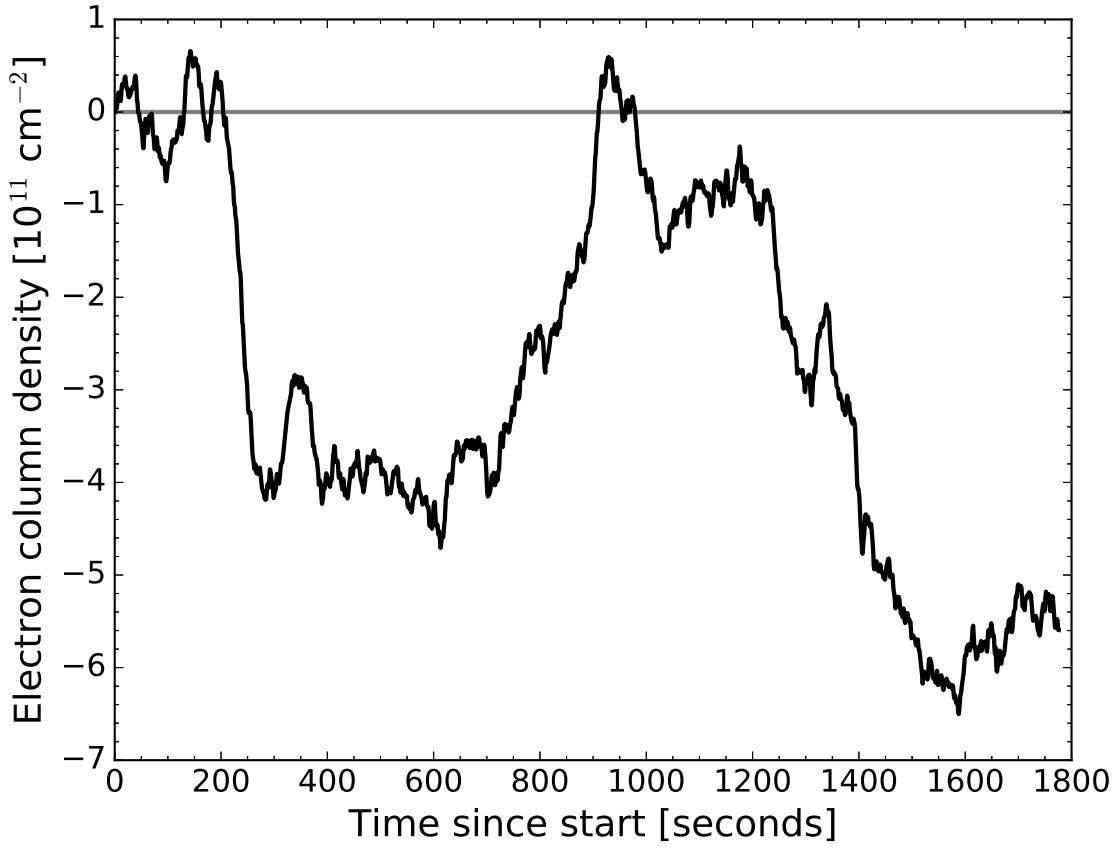

Figure 8: Time series of total electron content from S-band and X-band observations at DSS-14 during occultation T012X. The vertical line indicates zero. The abrupt change in total electron content at 200 seconds indicates the ionosphere. Note that 10^{11} cm^{-2} equals 10^{15} m^{-2}.

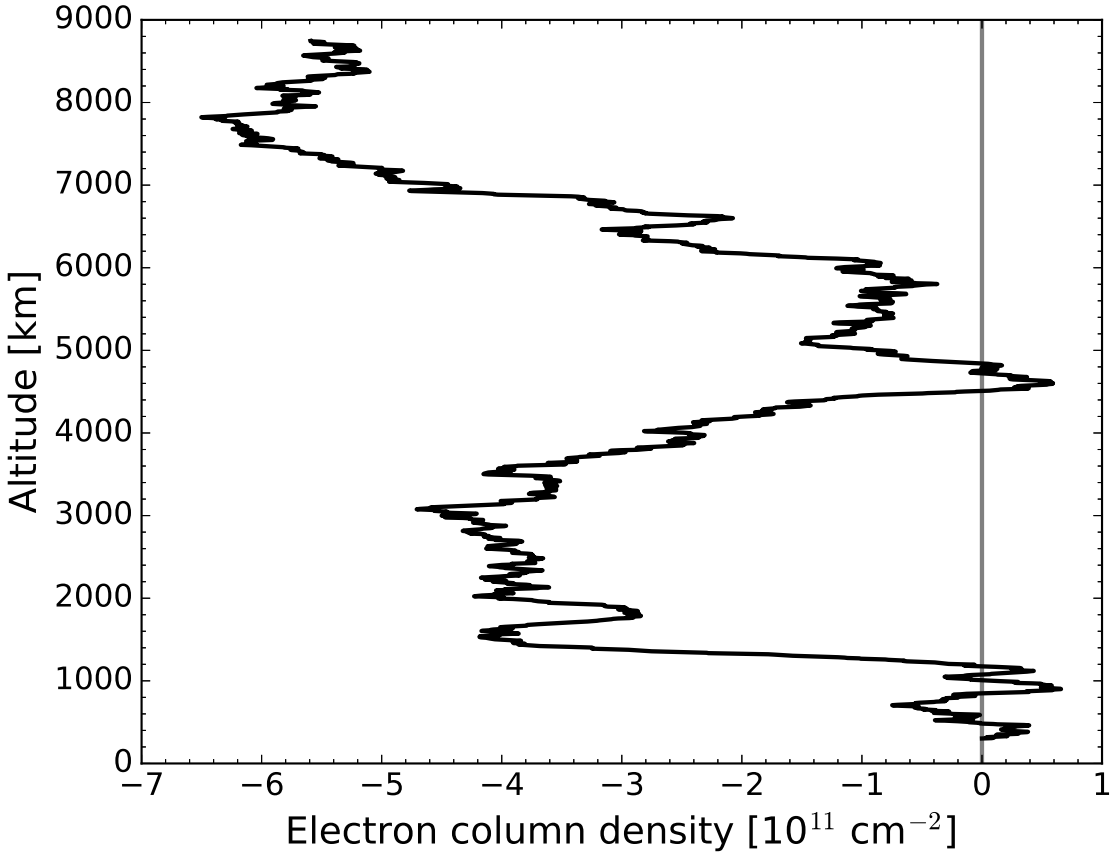

Figure 9: Vertical profile of total electron content from S-band and X-band observations at DSS-14 during occultation T012X. Zero is arbitrary. The abrupt change in total electron content at 1200 km altitude indicates the ionosphere. Note that 10^{11} cm^{-2} equals 10^{15} m^{-2}.

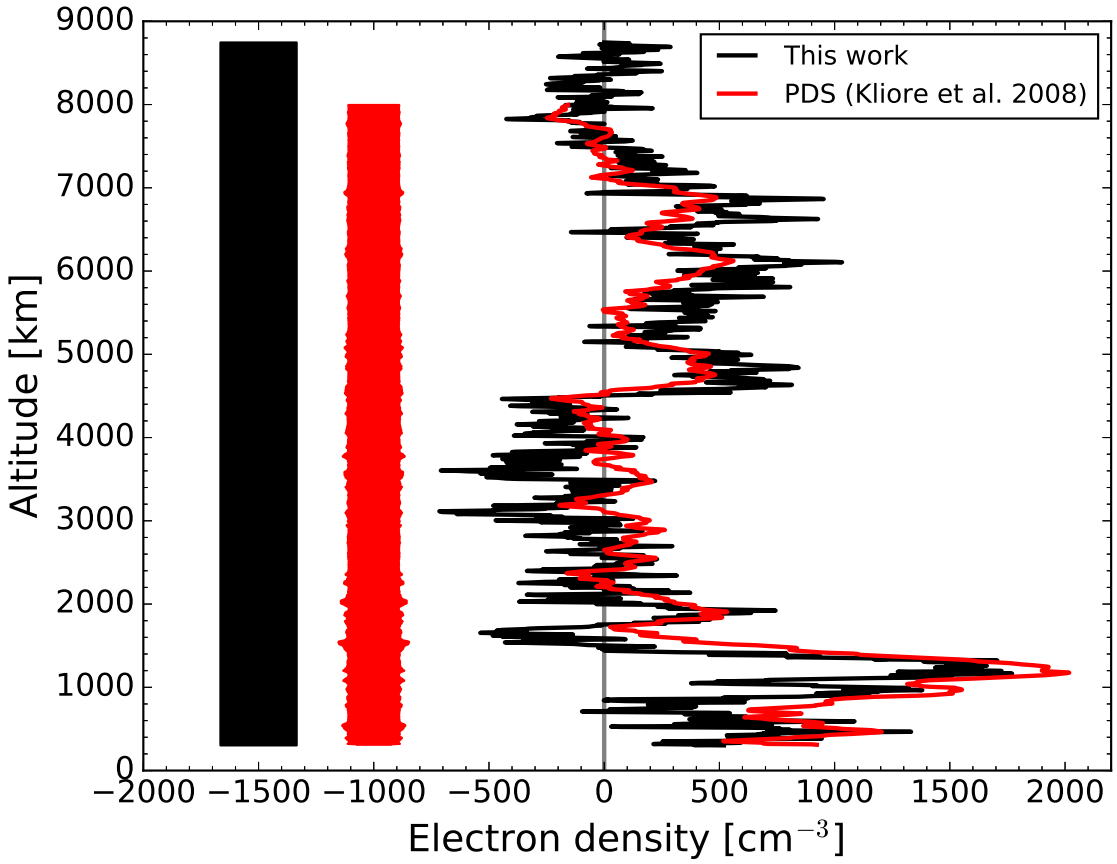

Figure 10: Electron density profile for occultation T012X. The black line shows the profile derived in this work from S-band and X-band observations at DSS-14. The red line shows the average profile reported by *Kliore et al.* (2008) and previously archived at the PDS. The width of the vertical bar indicates the 1-σ uncertainty in corresponding electron density profile. Uncertainty varies with altitude for the profile found by *Kliore et al.* (2008), but does not for the profile derived in this work. The grey vertical line marks zero.

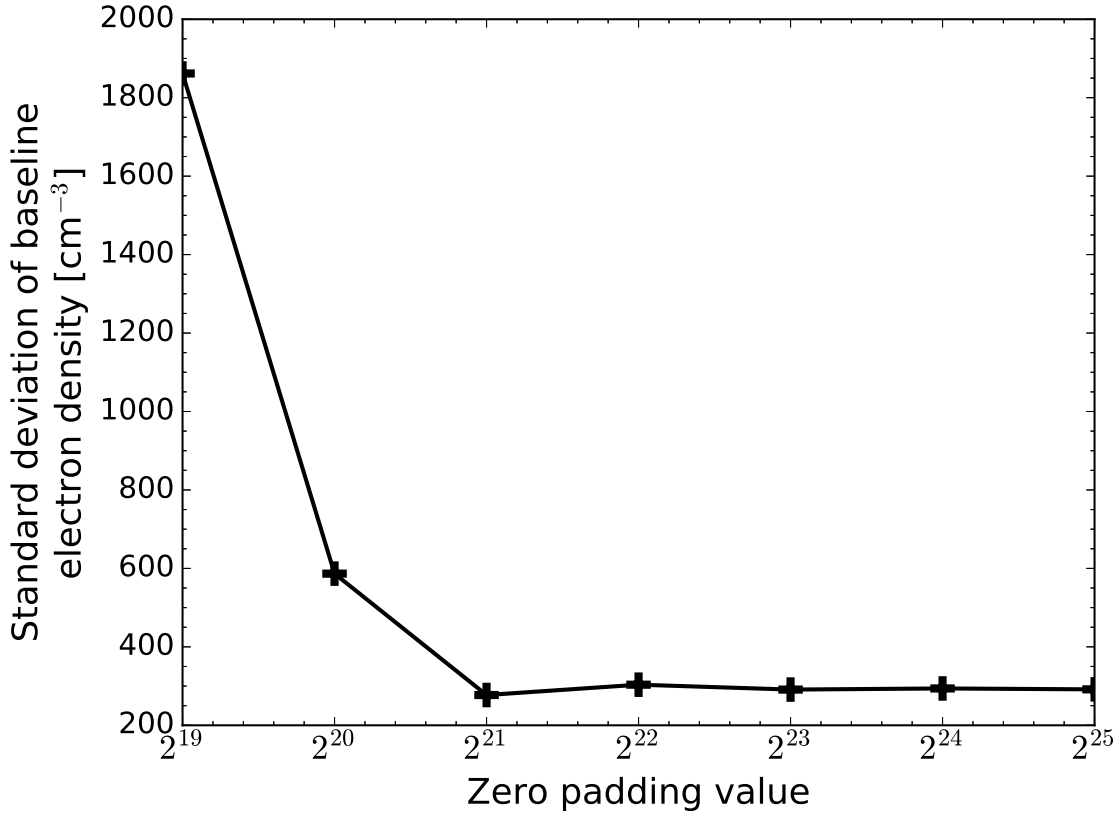

Figure 11: Electron density uncertainties in the electron density profile derived from S-band and X-band observations at DSS-14 during occultation T012X. Dependence of uncertainties on length of zero padding is shown.

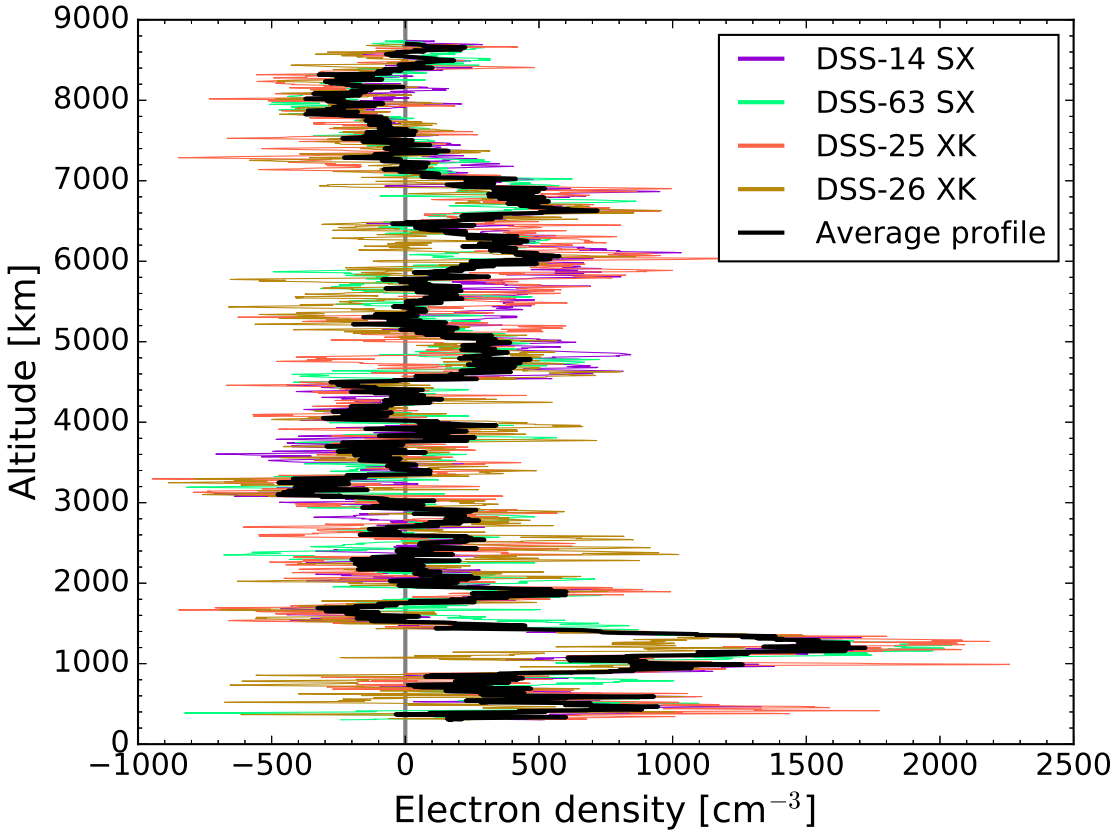

Figure 12: The four individual electron density profiles found for T012X. Colors correspond to profiles derived from observations at different DSN antennas as listed in the legend, where "SX" means S-band and X-band observations and "XK" means X-band and Ka-band observations. The average profile is also shown (black line).

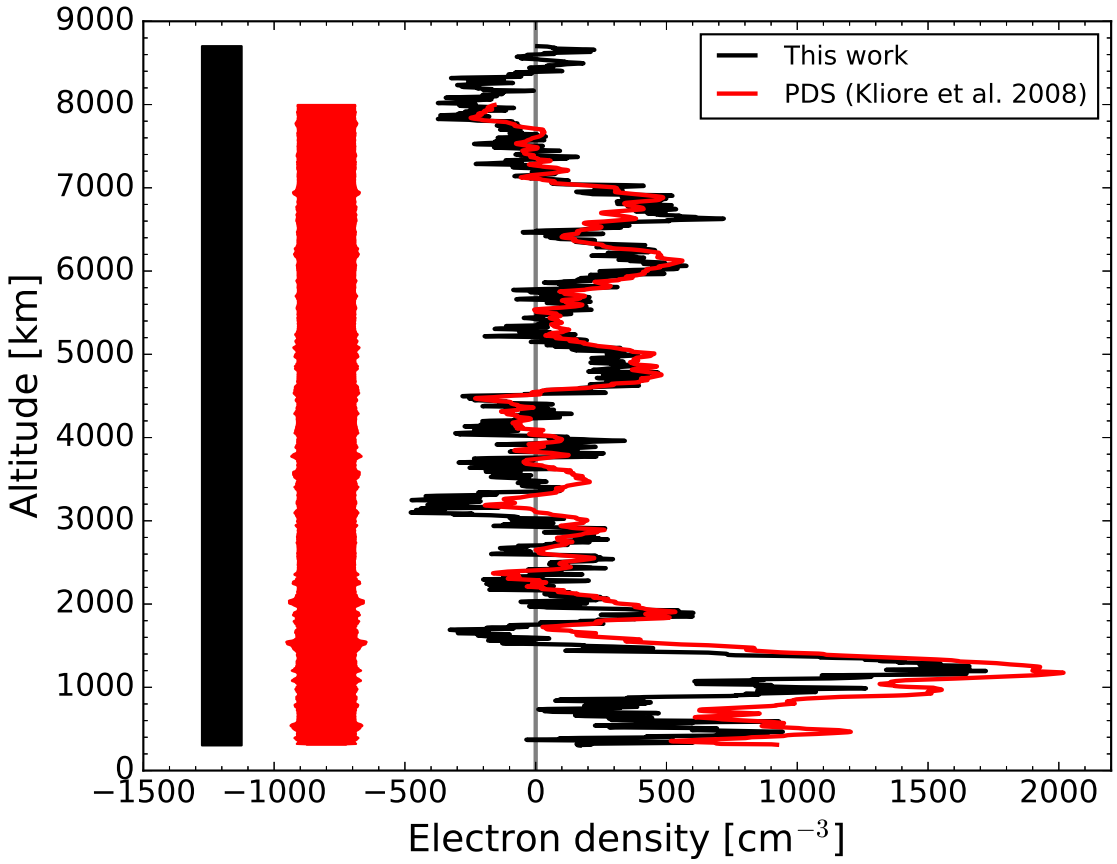

Figure 13: Electron density profile for occultation T012X. The black line shows the average profile derived in this work. The red line shows the average profile reported by *Kliore et al.* (2008) and previously archived at the PDS. The width of the vertical bar indicates the 1-σ uncertainty in corresponding electron density profile. Uncertainty varies with altitude for the profile found by *Kliore et al.* (2008), but does not for the profile derived in this work. The grey vertical line marks zero.

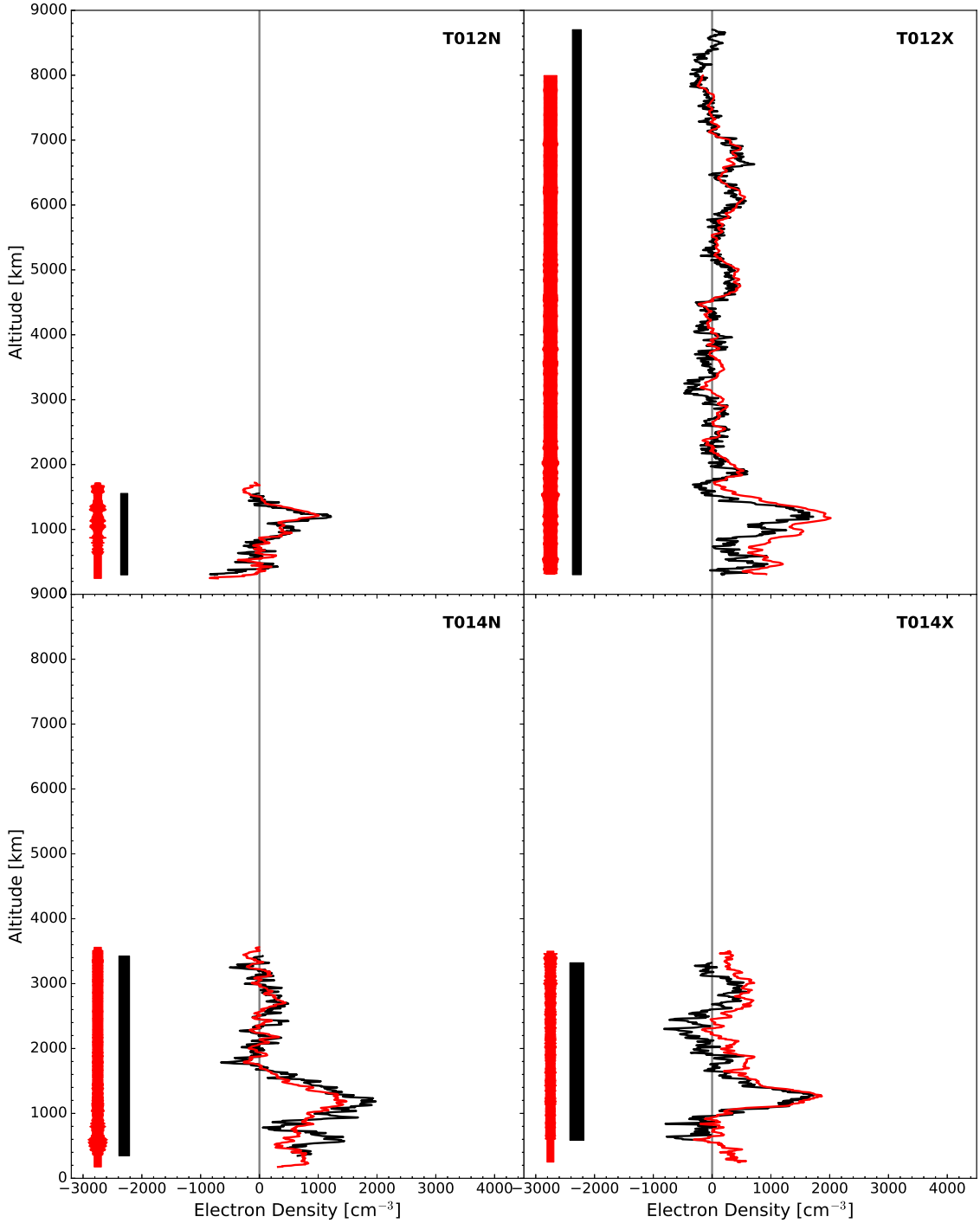

Figure 14: Electron density profiles for occultations T012N, T012X, T014N, and T014X. The black line shows the average profile derived in this work. The red line shows the average profile reported by *Kliore et al.* (2008) and previously archived at the PDS. The width of the vertical bar indicates the 1-σ uncertainty in corresponding electron density profile. Uncertainty varies with altitude for the profile found by *Kliore et al.* (2008), but does not for the profile derived in this work. The grey vertical line marks zero.

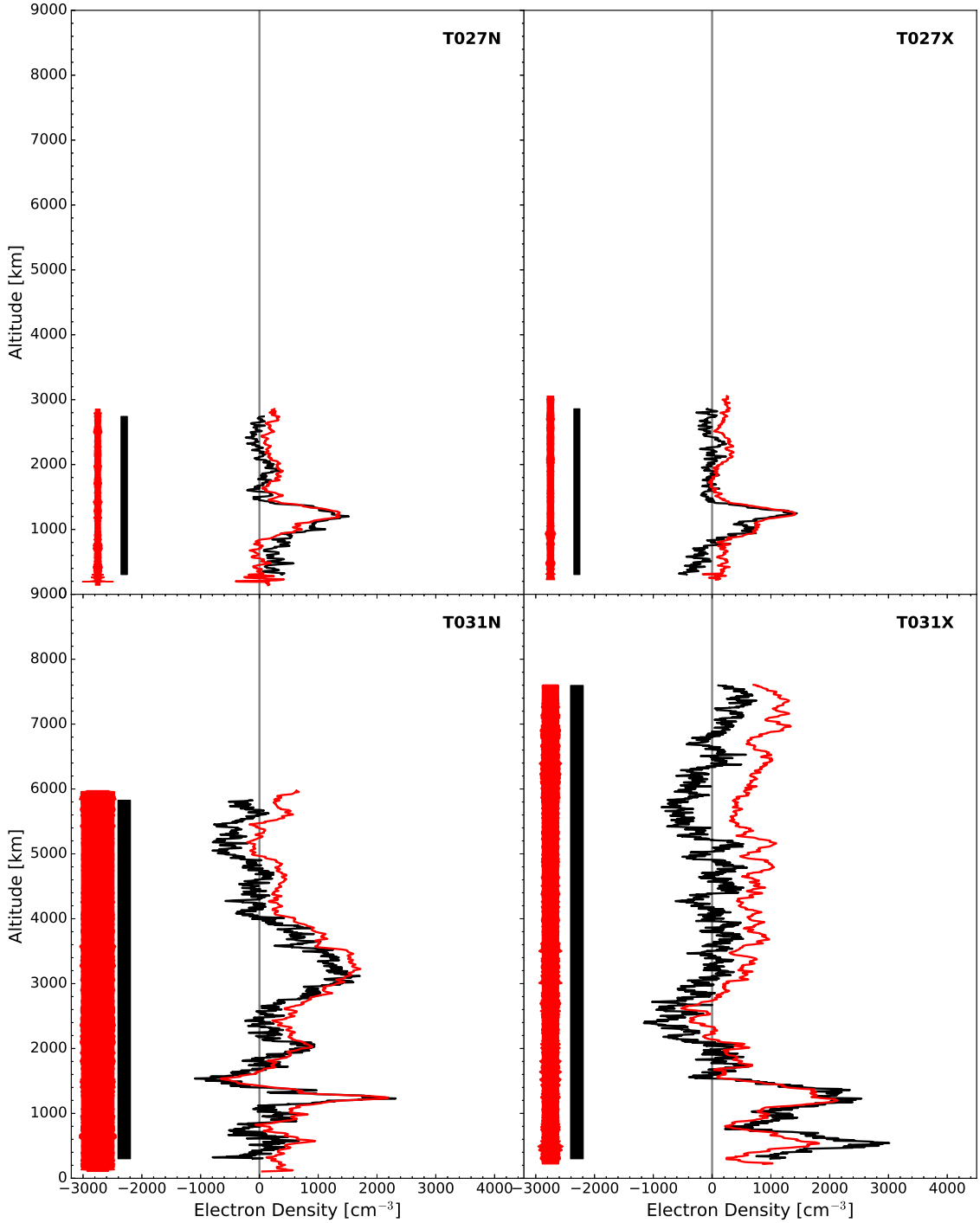

Figure 15: Electron density profiles for occultations T027N, T027X, T031N, and T031X. The black line shows the average profile derived in this work. The red line shows the average profile reported by *Kliore et al.* (2008) and previously archived at the PDS. The width of the vertical bar indicates the 1-σ uncertainty in corresponding electron density profile. Uncertainty varies with altitude for the profile found by *Kliore et al.* (2008), but does not for the profile derived in this work. The grey vertical line marks zero.

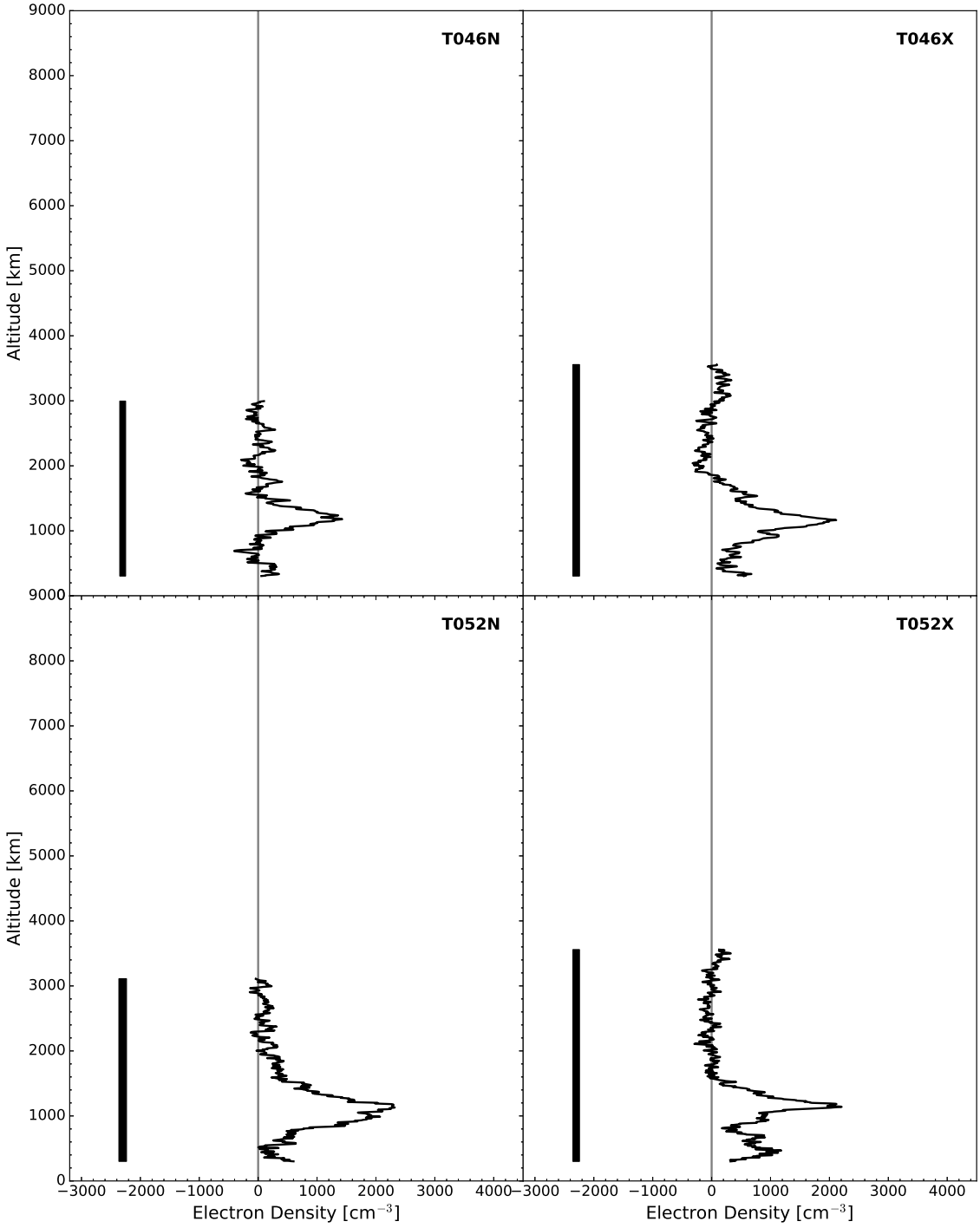

Figure 16: Electron density profiles for occultations T046N, T046X, T052N, and T052X. The black line shows the average profile derived in this work. The width of the vertical bar indicates the 1-σ uncertainty in corresponding electron density profile. The grey vertical line marks zero.

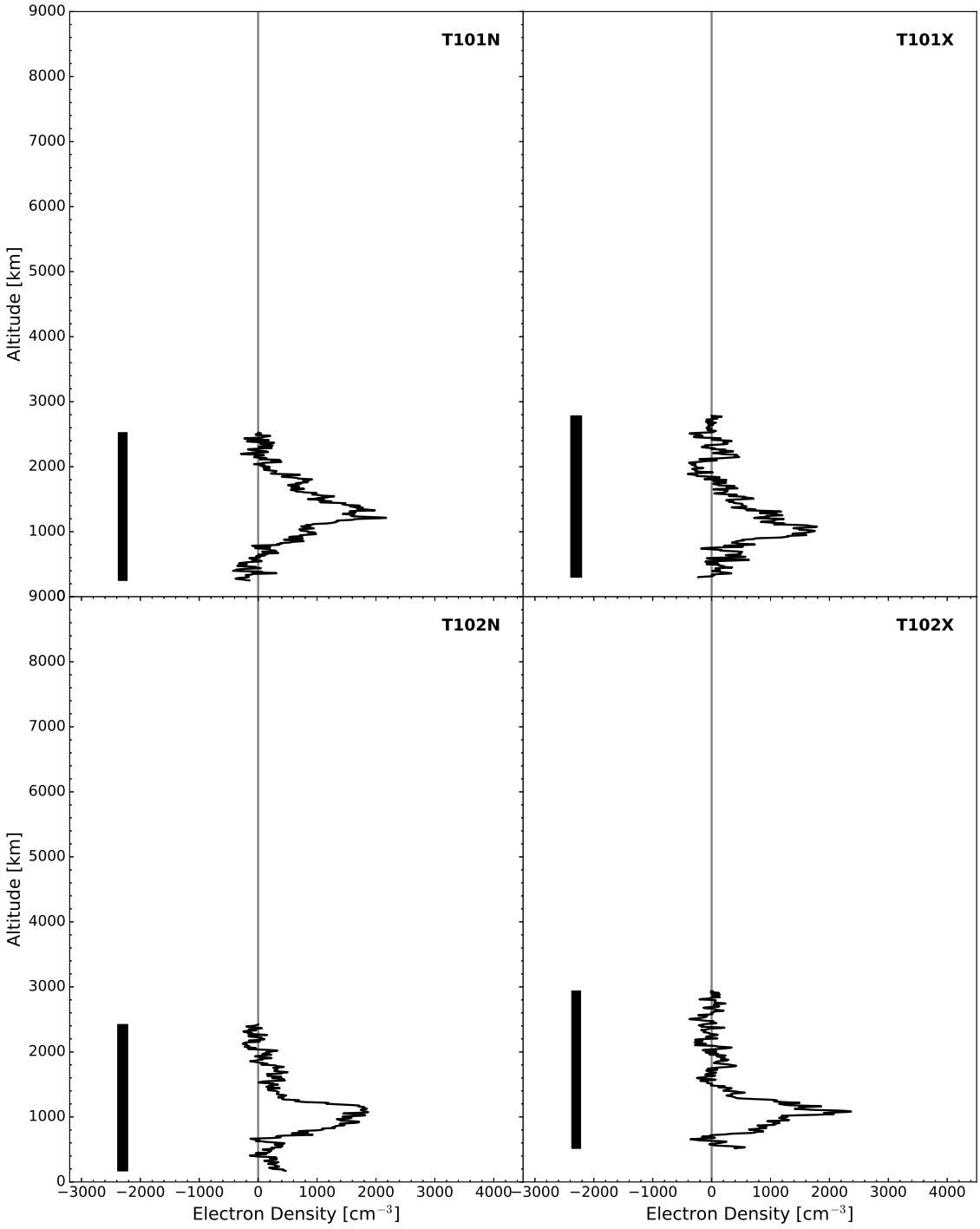

Figure 17: Electron density profiles for occultations T101N, T101X, T102N, and T102X. The black line shows the average profile derived in this work. The width of the vertical bar indicates the 1-σ uncertainty in corresponding electron density profile. The grey vertical line marks zero.

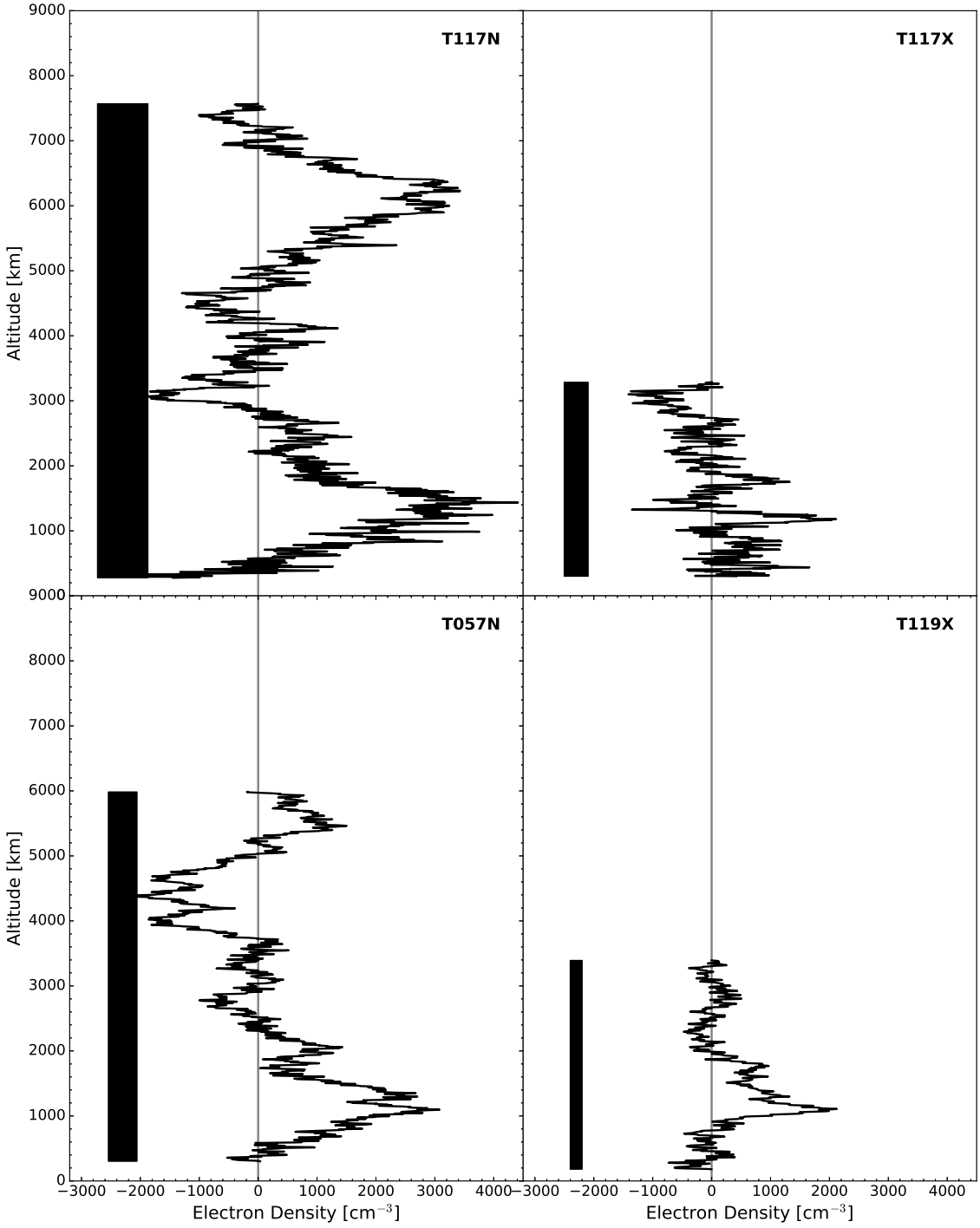

Figure 18: Electron density profiles for occultations T117N, T117X, T057N, and T119X. The black line shows the average profile derived in this work. The width of the vertical bar indicates the 1-σ uncertainty in corresponding electron density profile. The grey vertical line marks zero.